Article

Parallel Plate Capacitor Model at the Nanoscale for Stable and Gigantic SERS Activity of the 4-MBA@R-AuNP−4-MBA@R-AuNP System

Published as part of the ACS Omega special issue "Celebrating the 25th Anniversary of the Chemical Research Society of India".

Amar Ghosh, Murugesan Panneerselvam, Sourav Mondal, Prasanta Das, Tukai Singha, Subhasis Rana, Luciano T. Costa, Biswarup Satpati, Suman Das, Ujjal Kumar Sur, and Dulal Senapati*

Read Online

ACCESS | Metrics & More | Article Recommendations | SI Supporting Information

ABSTRACT: Selective use of ingredients out of a specific natural product (e.g., fruit, leaf, flower, or honey extract) or their mixture (e.g., bacteria, viruses, fungi, plants, etc.) by smart manipulation of precursors and reaction conditions to synthesize nanoparticles can provide us a low-cost, environmentally friendly route for their industrial-scale production. The presence of more than one active ligand (sourced natural product extract) on the surface not only makes them the most stable (electrostatically) and monodispersed (controlled kinetics) but also devoid of any external ligand-assisted aggregation. This empowered us to modify the surface of the nanoparticles in a monolayered fashion or to couple between nanoparticles through a ligand-assisted chemical coupling pathway to avoid their aggregation and hence to keep their nanoscale property intact. A metal-to-ligand charge transfer (MLCT) trajectory combined with electromagnetic field-induced coherent capacitive coupling between two nanoparticles was introduced to explain the gigantic Raman enhancement observed from these nanoparticles. As a model system, we have synthesized the nanoparticles from rose extract as the active ligand ingredient source for 2-phenyl ethanol, linalool, citronellol, nerol, geraniol, pyrogallol ($C_6H_3(OH)_3$), and quercetin (3,3′,4′,5,7-pentahydroxyflavone) and the surface of the synthesized nanoparticles has been modified by 4-mercaptobenzoic acid (4-MBA) acting as a Raman tag. The obtained structural and spectroscopic data correlate well between our numerical and density functional theory (DFT)-based calculations to justify their gigantic SERS activity, which may lead us to propose an unexplored coherent capacitive coupling-based Raman enhancement mechanism.
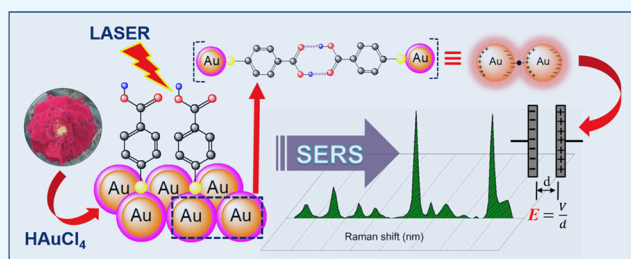
1. INTRODUCTION

Surface-enhanced Raman scattering (SERS) is a powerful, sensitive, selective, and label-free molecular spectrometric technique not only for quantitative identification but also to understand the structure, orientation, and adsorption of a molecule on a surface.[1−6] After its invention in the early 1970s,[7−11] in the last 50 years, researchers primarily explained SERS as the result of (i) electromagnetic enhancement (associated with the excitation of intense and sharp localized surface plasmons) and (ii) chemical enhancement (associated with the metal-to-molecule or molecule-to-metal charge transfer to dramatically alter the resonance condition of the system).[12] Although Raman scattering is typically a weak effect, making it challenging to detect low concentrations of molecules or molecules with weak Raman scattering cross-sections ($\sim 10^{-30}$ cm^2 molecule^{-1}),[13] SERS enhances the Raman scattering signal by many orders of magnitude through interactions between the molecules and a roughened metallic surface (typically gold or silver nanoparticles) or nano-structured surfaces (such as roughened metal films or metal-coated nanoparticles). By considering that electromagnetic enhancement (EM) and chemical enhancement (CM) are the two most effective and well-studied enhancement mechanisms, the four most important factors that account for the measurable SERS enhancement (G) are as follows: (a) scattering by the metal particle rather than by the Raman-active molecule contributes majorly to SERS, (b) although G varies as the fourth power of the local incident near-field, the intensity of SERS linearly varies with the intensity of the incident field, (c) SERS intensity is proportional to the

polarizability of the adduct (Raman-active molecule adsorbed on the nanoparticle) rather than the Raman-active molecule only, and (d) SERS is a near-field phenomenon. Here, factors (c) and (d) mostly account for the contribution of CM and EM, respectively. The conceptual formulation of G is well elaborated by Moskovits.[11,12] Beyond EM and CM mechanisms, there are few other mechanisms seldom mentioned in the literature, and not many reported studies are based on these mechanisms. These rare mechanisms include (A) the polarizability enhancement mechanism[14] and (B) the coherent capacitive coupling (CCC) enhancement mechanism.[12] Both of these enhancement mechanisms are based on the dipolar polarization of the Raman-active molecule and nanoparticle. The main target of this work is to perform experimentation and to search for a theoretical explanation to understand these two mechanisms of SERS enhancement in detail. A solid knowledge of the mechanism of Raman signal enhancement will help us to apply SERS as a viable technique in various fields, including analytical chemistry,[15] biochemistry,[16] and materials science.[17] Further, its ultrasensitivity and high specificity for various functional groups (a group of atoms in a molecule with distinctive chemical properties, regardless of the other atoms in the molecule) allow us to use SERS for the trace-level detection and identification of molecules in an unknown sample, making it valuable in sensing applications.[18] In addition, SERS has been continuously evolving, and there have been several recent applications across various fields such as biomedical sensing and imaging,[19] environmental monitoring,[20] food safety and quality control,[21] forensic analysis,[22] drug delivery,[23] and therapeutics[24] to the detection of biomolecules, imaging cellular processes, and studying interactions at the molecular level. However, challenges in SERS include the reproducibility of signals, background interference, and optimization of substrates for specific applications. Recent advances in SERS research focus mostly on the development of novel substrates[25−28] and surface modifications[29,30] to overcome these challenges and further expand the capabilities of the technique.[31−33] Unfortunately, most of the available reports try to explain the observed SERS spectra and their sensitivity based on the EM and CM mechanism. In that direction, few notable reports[11,12,34,35] are available in the literature where a different mechanism has been introduced to explain the observed enhanced Raman signal on a nanosurface when they fail to explain by the existing mechanisms. Very recently, Senapati et al.[36] have applied the CCC enhancement mechanism in this perspective to explain the Raman signal enhancement originating from Rh6G adsorbed on "multiple gold nanoparticle cores within a single SiO$_2$ shell".

To understand more about the CCC enhancement mechanism, in this work, we have fabricated a biogenic gold nanoparticle (AuNP) by using rose petal extract as the active natural source of multiple surfactants. These rose extract-mediated AuNPs (R-AuNPs) were characterized using ultraviolet−visible (UV−vis) absorption spectroscopy, attenuated total reflectance Fourier transform infrared spectroscopy (ATR FT-IR), X-ray diffraction (XRD), dynamic light scattering (DLS), and field emission-scanning electron microscopy (FESEM) as well as high-resolution transmission electron microscopy (HRTEM) studies to understand their structural, compositional, and ligand binding behavior. Multicomponent natural extract as a surfactant helps mold the nanoparticle surface in such a way that the external addition of a thiolated

aromatic compound (4-mercaptobenzoic acid [4-MBA], 4-aminothiophenol [4-ATP], and 4-methylbenzenethiol [4-MBT]) makes a self-assembled monolayer (SAM) on the nanoparticle either remain as isolated particles or make an intermolecular hydrogen bond between nearby nanoparticles without making any aggregation. The addition of an increasing concentration of the thiolated aromatic compound makes an enhanced possibility of intermolecular hydrogen bonding between nearby nanoparticles, which may result in a sharp transition in SERS signal intensity with the concentration. Moreover, a series of nonthiolated ligands (4-aminobenzamide [4-AB], 4-aminobenzoic acid [4-ABA], and 1,4-diaminobenzene [1,4-DAB]) have also been tested as a Raman tag to validate our proposed mechanism of coupled nanoparticles through intermolecular hydrogen bonding for gigantic Raman signal enhancement. In the discussion section, we explain the mechanism of the formation of coupled nanoparticles only for 4-MBA, which is responsible for generating CCC between two nearby nanoparticles upon plasmonic excitation. A density functional theory (DFT) level calculation has been performed for the optimization of different ligands on the nanoparticle (10-atom AuNP) surface and optimization of thiol and thiolate of 4-MBA to measure the highest occupied molecular orbital (HOMO)−lowest unoccupied molecular orbital (LUMO) energy gap as well as to estimate the charge transfer ability. Optimization of dimeric 4-MBA on nanoparticles has also been performed to compare the extent of charge transfer compared with isolated ligand (4-MBA)-coated nanoparticles. Moreover, we have used the DFT calculation to understand the nature of charge transfer (between metal-to-ligand charge transfer (MLCT) and ligand-to-metal charge transfer (LMCT)). Theoretically, we have also checked the variation of the HOMO−LUMO band gap as a function of the electric field gradient to understand the role of the size of the nanoparticle. Since the interparticle distance is governed by intermolecular hydrogen bonding, the field gradient remains almost constant for a specific nanoparticle if it shows a monodispersive nature. A systematic study of the photoinduced charge transfer (PICT) in the SERS signal of 4-MBA on the impact of intermolecular H-bonding in the plasmonic molecular pair junction was carried out, getting to the large enhancement in the SERS signal around the order of ∼10^7. In turn, we developed a new concept/theory about the CCC enhancement mechanism by studying the metal−adsorbate molecule system, through charge redistribution and orientation on the AuNP surface in the presence of applied laser energy. This prototype system will help us to generalize a strategy for gigantic Raman signal enhancement for highly specific and ultrasensitive detection platforms for unknown analytes. The new invention of this work that gives a theory about SERS enhancement can indeed be integrated into a capacitor structure through dipole-induced polarization. In a capacitor structure, the dipole-induced polarization effect can be leveraged to enhance the local electric field around the SERS-active substrate. This enhanced electric field, in turn, increases the Raman scattering cross-section of molecules in the proximity of the substrate, leading to stronger Raman signals.

From a chemist's point of view, although the bottom-up synthesis of nanoscale materials by using a single-component pure ligand as the surfactant is the most common methodology used in the literature, utilization of biological ingredients (sourced from microorganisms, plants, insects, etc.) to synthesize biofriendly nanoparticles is on the rise. As a rich

source of phenols, flavonoids, alkaloids, etc., bioingredients act both as reducing and stabilizing agents that principally improve the monodispersity, size tunability, and time efficiency.[37−42] Out of the various nanoscale materials, AuNPs are of great interest owing to their extraordinary physical and chemical properties and their potential applications due to their inertness, higher stability, and less toxicity. Application of rose (*Rosa damascena*) plant extract for the green synthesis of AuNPs[38,43−46] is on the rise because of its known resources of phenols (ellagic acid, catechol, resorcinol, gallic acid, and phloroglucinol), flavonoids (luteolin, apigenin, quercetin, rutin, kaempferol, and chrysoeriol), and alkaloids (berbamine, jatrorrhizine, palmatine, reticuline, isocorydine, and boldine).

To understand the role of charge transfer and electromagnetic field-driven dipole-induced capacitive coupling between nanoparticles through intermolecular hydrogen bonding, we have considered 4-MBA as a model system, capable of making a covalent bond on the nanoparticle surface as well as remaining bonded with another 4-MBA-coated nanoparticle through intermolecular hydrogen bonding, by comparing with other thiolated aromatic ligands (4-ATP and 4-MBT) incapable of making intermolecular hydrogen bonding or resulting in a much weaker H-bond and nonthiolated aromatic ligands (4-AB, 4-ABA, and 1,4-DAB) incapable of making a gold−thiol bond for effective adsorption. Our newly synthesized biocompatible nanoparticle also shows great Raman signal enhancement for various positively charged dyes (crystal violet, rhodamine B, rhodamine 6G, and Congo Red) and hence can be used as a traditional SERS platform.

2. EXPERIMENTAL SECTION

2.1. Materials. Chemicals including gold chloride trihydrate (HAuCl$_4$·3H$_2$O, ≥99.9%, trace metal basis), 4-mercaptobenzoic acid (4-MBA, C$_7$H$_6$O$_2$S, technical grade, ≥98%), 4-aminothiophenol (4-ATP, C$_6$H$_7$NS, ≥97%), 4-methylbenzenthiol (4-MBT, C$_7$H$_8$S, ≥98%), 4-aminobenzamide (4-AB, C$_7$H$_8$N$_2$O, ≥98%), 4-aminobenzoic acid (4-ABA, C$_7$H$_7$NO$_2$, ≥99%), 1,4-diaaminobenzene (1,4-DAB, C$_6$H$_8$N$_2$, ≥99%), rhodamine 6G (Rh6G, dye content ≥92%), rhodamine B (Rh−B, dye content ≥95%), crystal violet (CV, dye content ≥90%), and Congo Red (CR, dye content ≥97%) were procured from Sigma-Aldrich chemicals Pvt. Ltd. (St. Louis, MO). All the chemicals and solvents (methanol, CH$_4$O, ≥97%) used in the present study were high-quality analytical grade or HPLC grade and used without further purification. Milli-Q water (Resistivity: 18.2 MΩ·cm at room temperature) was used in preparing solutions.

2.2. Preparation of the Rose Petal Extract. Fresh rose flowers (*R. damascena*) were collected from the Saha Institute of Nuclear Physics campus (22.58018° N, 88.39165° E), Kolkata, India, and the rose petals were washed precisely with tap water followed by Milli-Q water. 5 g of the crushed air-dried flower was taken in 250 mL Erlenmeyer flasks with 100 mL of Milli-Q water and refluxed with a condenser keeping a constant water flow, on a magnetic heater−stirrer at 80 °C for 30 min with constant stirring as illustrated in the Supporting Information (SI) section (Scheme S1). The resulting aqueous flower extract was cooled to room temperature, followed by filtering through Whatman grade 41 filter paper. The filtrate (pink in color) was stored at 4 °C and was further employed for the synthesis of gold nanoparticles (AuNPs).

2.3. Synthesis of Au Nanoparticles. A 5 mL portion of 10^{-2} M aqueous HAuCl$_4$ solution was mixed with 0.25 mL of

aqueous rose flower extract under constant stirring (at 200 rpm) at room temperature in a 20 mL glass vial. The resultant reaction mixture is then kept for 1 h at room temperature for the growth of nanostructures. A gradual color change from light yellow to deep pink indicates the formation of nanoparticles (R-AuNPs) as shown in Scheme S1. Once the color of the nanoparticle solution stabilized, we centrifuged the whole solution at 5000 rpm for 30 min to separate out nanoparticles from other unreacted ingredients.

2.4. UV−Vis Absorption Spectroscopy. The measurement of UV−vis absorption spectra of these newly synthesized nanomaterials (R-AuNPs) and their different R-AuNP-ligand as well as R-AuNP-dye complexes was carried out to understand the binding properties of different ligands and dye molecules on the nanoparticle surface. Absorption spectra of bare R-AuNPs give an idea of their size, shape, and composition. For all measurements, we used a JASCO-V650 UV−vis-NIR spectrometer within the wavelength range of 900−200 nm.

2.5. Hydrodynamic Size and Surface Charge of Nanoparticles. Dynamic light scattering (DLS) studies to get an idea about the hydrodynamic radii and ζ-potentials to understand the surface charge of these nanomaterials were performed by using a Malvern-made Zetasizer Nano ZS90 instrument.

2.6. Electron Imaging. The TEM and HRTEM measurements were done using a Tecnai G2 F30 S-Twin microscope operating at 300 kV made by FEI. A HAADF detector from Fischione Model-3000 was used for high-angle annular dark-field scanning (STEM-HAADF). Elemental mapping and compositional analysis were done by energy-dispersive X-ray spectroscopy (EDX) on a Tecnai G2 F30S-Twin microscope.

2.7. Infrared Spectroscopy in the Solution Phase. The concentrations of pure rose extract (a mixture of various ligands with unknown concentration) and rose extract used for nanoparticle synthesis are taken as the same for the infrared spectroscopic measurement. Similarly, the concentration of 4-MBA alone and 4-MBA in the NP-MBA mixture is fixed at 0.9 × 10^{-3} M. IR spectra were recorded in the 4000−500 cm^{-1} range with 2 cm^{-1} spectral resolution and an average of over 128 scans, using a single-pass universal attenuated total reflectance (ATR) cell coupled with an FT-IR spectrometer (α II, Bruker Optics). For measuring IR spectra, about 50 μL of solution was placed and protected with a convex coverslip. The solvent water or water−methanol mixture was used for background spectra.

2.8. SERS Measurements. Before each SERS measurement, we mix 20 μL of centrifuged R-AuNPs with 180 μL of 10^{-3} M Raman-active molecules (v/v) and homogenize further. A 2 mL polypropylene-made centrifuge tube cap was used as the sample chamber to hold a 200 μL Raman-active sample for all SERS measurements. The analytes were excited by using a DPSS laser operating at 671 nm. Throughout the experiments, we used 20 s acquisition time with laser power in the range of 2−5 mW. For each set of experiments, we have repeated the experiment at least three times.

A detailed characterization of R-AuNPs is discussed in the SI section as Figure S1.

2.9. Computational Details. Density functional theory (DFT) calculations for molecular structure optimization and Raman spectrum calculations on the chosen molecules were carried out using Gaussian 09 software.[47] The calculations involved varying applied electric fields, ranging from 0 to 0.26
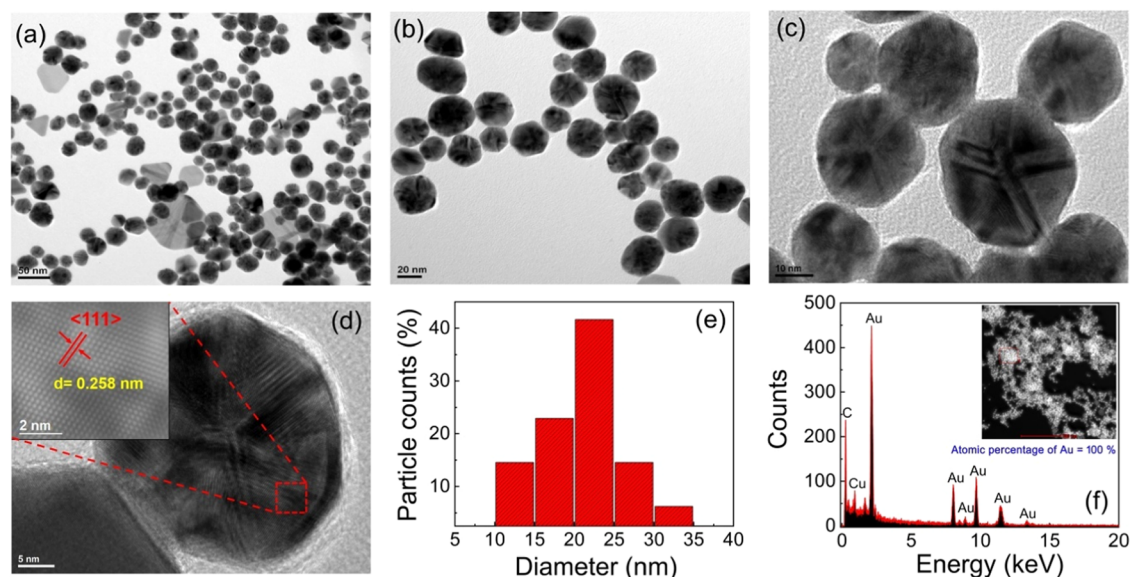
Figure 1. (a−c) TEM images of the synthesized gold nanoparticles with different magnifications, (d) HRTEM image of single spherical nanoparticles showing lattice planes with a spacing of 0.258 nm corresponding to (111) Bragg's plane, (e) particle size distribution of R-AuNPs obtained from TEM analysis, and (f) EDX spectrum of the biosynthesized AuNPs.

V Å^{-1}. Also, DFT calculations were employed to fully optimize the geometries of all molecules featuring Au clusters in their neutral states. This optimization utilized Becke's three-parameter exchange and correlated functional with Lee−Yang−Parr correlation (B3LYP hybrid exchange−correlation), incorporating the dispersion D3-corrected B3LYP-D3[48,49] functional alongside 6-31G(d)[50] basis sets under vacuum conditions. Specifically, the 6-31G(d) basis set was allocated to C, H, N, O, and S atoms, while the Los Alamos National Laboratory 2 Double-Zeta (Lanl2DZ)[51,52] basis set was applied to gold atoms. Theoretical calculations were conducted to predict the IR and Raman spectra of the molecule. Additionally, experimental Fourier transform infrared (FTIR) and Raman spectra were obtained for the compound. The computed results obtained at the B3LYP/6-31G(d)/Lanl2DZ level facilitated the assignment of all FTIR and Raman bands observed experimentally. Our calculated vibrational frequencies demonstrated a close match with the experimental values, indicating a high level of agreement. Additionally, we performed an analysis of the highest occupied molecular orbital (HOMO) and lowest unoccupied molecular orbital (LUMO) levels, assessing the HOMO−LUMO gap through frontier molecular orbital (FMO) analysis.[53] Additionally, we examined the binding adsorption energy (ΔE) and investigated the charge transfer processes within the Au(0)-thiol and Au(1)-thiolate molecular compounds. The binding adsorption energy (ΔE) was calculated using eq 1[54−56]

$$\Delta E = E(\text{product}) - \Sigma[E(\text{reactants})] \qquad (1)$$

where $E(\text{product})$ is the total energy of different ligands on surface-catalyzed R-AuNPs and $\sum(\text{reactants})$ is the sum of the total energies of the Au surface and 4-MBA, 4-MBT, 4-ATP, 4-AB, 4-ABA, and 1,4-DAB with Au(0)-thiol and Au(1)-thiolate clusters. Moreover, the mechanism of molecules adhering to a metal surface is influenced by various factors, such as the interaction dynamics between the substrate and the molecule, which involve electrostatic forces, van der Waals forces, and π−π stacking forces.[54,57] Additionally, the involvement of SAMs and the surrounding environment significantly impacts

this adsorption process. These aspects were further explored through the investigation of intermolecular noncovalent interactions (NCIs) using the multifunctional wave function analyzer (Multiwfn).[58]

3. RESULTS AND DISCUSSION

The absorption spectra (Figure S1a) of the synthesized R-AuNPs show two clear surface plasmon resonance (SPR) bands at 527 and 666 nm. The more intense SPR band at 527 nm corresponds to the formation of spherical AuNPs, whereas the less intense SPR broad band at 666 nm indicates the formation of anisotropic nanostructures like nanotriangles, nanopentagons, and nanohexagons, as clearly observable from the TEM images shown in Figure 1a. A brief description of the dependency of the position, wavelength shift, full width at half maxima (fwhm), and the number of plasmon bands in the absorption spectra of a synthesized plasmonic nanoparticle on its size, shape, composition, and its polydispersity nature is included in the SI section. Magnified TEM images of the same spherical nanoparticles are shown in Figure 1b,c. As the nanoparticle synthesis progresses, a broad absorption peak centered at 500 nm, originating from the rose petal extract, gradually disappears and results in an intense peak at 527 nm, indicating the formation of rose extract-encapsulated gold nanoparticles (R-AuNPs) by utilizing rose petal extract as an active surfactant.

The morphology and size of R-AuNPs are analyzed by transmission electron microscopy studies. The obtained TEM image (Figure 1a−c) infers that most AuNPs are mono-dispersed, spherical in shape. A certain percentage of particles with triangular and hexagonal shapes are also visible in Figure 1. The calculated lattice spacing of 0.258 nm from HRTEM analysis corresponds to the (111) lattice planes of face-centered cubic (fcc) gold (Figure 1d). Particle size distribution as shown in Figure 1e shows an average diameter of ∼22 nm. The absolute size and shape of the R-AuNPs are also verified by scanning electron microscopy (SEM) measurements. The SEM measurements confirm that all particles are spherical,

homogeneous, and monodispersed (with a diameter of ~22 nm) in nature as shown in Figure S2. The presence of Au as a single metal element with 100% atomicity in the synthesized nanoparticles is confirmed by the measurement by EDX analysis (Figure 1f). The fcc structure of R-AuNPs is also confirmed by the XRD study (Figure S1b), which shows four diffraction peaks at 2θ values of 38.09, 44.15, 64.67, and 77.54°, which are indexed to the (111), (200), (220), and (311) Bragg's reflection planes, respectively. The obtained data are matched with JCPDS card no. (65−2871), and the sharpness of peaks evidently revealed that particles are crystalline in nature.[38] The crystallite diameter of the obtained R-AuNP is calculated to be 19.4 nm by using the Debye− Scherrer equation $\left(D = \frac{k\lambda}{\beta \cos \theta}\right)$, where D is the crystallite diameter, k is Scherrer's constant (0.89 for spherical-shaped particles), λ is the wavelength (nm) of X-ray, θ is Bragg's angle in radians, and β is the full width at half maximum (fwhm) in radians of the most intense (111) peak. The obtained result matches well with the average diameter obtained from the TEM analysis.

The hydrodynamic radius of the synthesized R-AuNP is evaluated from dynamic light scattering (DLS) measurements. The average diameter of nanomaterials is found to be 35.5 nm as shown in Figure S1c. A deviation in the diameter value obtained between DLS and TEM (measured absolute diameter) indicates the ionic nature of the nanoparticle. The larger the deviation, the greater the ionic nature and vice versa. The surface charge of R-AuNPs is found to be ~−43.1 mV from the measurement of zeta potential (ξ), shown in Figure S1d. The high value of ξ confirms good stability (weeks) of our synthesized R-AuNPs at room temperature due to the strong repulsive force between charged R-AuNPs to prevent aggregation. As described in Section 1, the negative (−ve) charge of R-AuNPs is attributed to the presence of biomolecules (phenols, flavonoids, alkaloids, etc.) in the rose extract, which are responsible for the efficient stabilization of R-AuNPs. The participation of various biomolecules and their fragments in the nanoparticle synthesis is confirmed by recording the FTIR spectra of rose petal extract and R-AuNPs. The presence of similar vibrational peaks in both the extract [3530.3 (w), 2948.2 (w), 2896.2 (w), 1730.7 (s), 1612.6 (s), 1351.4 (s), 1224.1 (w), 1204.6 (s), 1103.3 (w), 1080.5 (s), and 1055.9 (s) cm^{-1}] and R-AuNPs [3176.2 (s), 2920.8 (s), 2851.3 (s), 1725.9 (w), 1625.5 (s), 1351.4 (w), 1260−1117 (w), and 1122−1000 (w) cm^{-1}], as shown in Figure 2, confirms the presence of the same biomolecules of the extract on the R-AuNP surface. Letters "s" and "w" in the

parentheses indicate the strong and weak IR bands, respectively. The IR band at 3530.3 cm^{-1} indicates the presence of a free −O−H bond (stretching) in the rose extract compared to the bound −O−H bond for R-AuNPs confirmed by a huge negative frequency shift combined with intensity enhancement. Similarly, IR bands for C−H stretching (at 2948.2 and 2896.2 cm^{-1}) and C=O stretching (at 1730.7 cm^{-1}) show a negative shift, while C=C stretching (at 1612.5 cm^{-1}) shows a positive shift for R-AuNPs. Shifting toward a lower frequency of different functional stretching vibrations indicates that −OH, −C−H, and C=O groups are directly involved in the reduction of Au(III) ions to transform into R-AuNPs. On the contrary, shifting toward higher frequency for C=C confirms the presence of aliphatic/aromatic alkene (C=C) groups on the R-AuNP surface in a π−π stacking configuration to increase its effective bond order. Moreover, a marked enhancement in intensity for −O−H and C=C stretching bands indicates a possibility of inter/intramolecular hydrogen bonding along with the π−π stacking configuration of the R-AuNP surface. A marked reduction in C=O stretching (at 1730.7 cm^{-1}) intensity may infer the non-involvement of C=O in the inter/intramolecular hydrogen bonding.

Once we synthesized these biogenic R-AuNPs, we adopted self-assembled monolayer (SAM, to create a well-defined, highly ordered molecular architecture) formation of probe molecules onto the surface of the R-AuNP to record their SERS signal. In general, molecules with a headgroup that interacts strongly with the metal surface and a tail group that dictates the properties of the monolayer form a stable SAM. Common molecules used for SAM formation include thiols, disulfides, phosphines, and cyanides. A more detailed illustration of the mechanism of SAM formation by 4-MBA on our synthesized R-AuNP is elaborated in the SI section (Scheme S2). In this work, we have used various aromatic ligands with or without thiol as the headgroup and a tail (functional) group for the molecular interaction with the nearby SAM-coated R-AuNP. Covalent adsorption of 4-MBA on the R-AuNP to form a stable SAM is again confirmed by recording the ATR FT-IR spectra of pure 4-MBA (0.9 × 10^{-3} M) and 4-MBA-coated R-AuNPs having the same concentration of the ligand (4-MBA). The possibility of unbound 4-MBA is removed by centrifuging the R-AuNP solution after SAM coating of 4-MBA. Overall, spectral patterns for both 4-MBA and the 4-MBA-coated R-AuNP are identical. An overall intensity enhancement of IR absorption bands for 4-MBA-coated R-AuNPs compared with free 4-MBA indicates a strong binding of 4-MBA on the R-AuNP surface. Moreover, a notable negative shift for −O−H and −S−H stretching vibrations indicates a ligand-induced substantial inter/intra-molecular hydrogen bonding. A very weak intensity originating from −S−H (stretching band at 2544.5 cm^{-1} and bending band at 848.0 cm^{-1}) may indicate a low possibility of the Au−S−H bond and mostly remains as thiolate (Au−S), which is also confirmed by our FMO calculation on the 4-MBA@Au$_{10}$ system. Unfortunately, the Au−S stretching band comes at ~260 cm^{-1}, which is not accessible in our α II, Bruker Optics ATR FR-IR spectrometer. A complete list of the vibrational bands observed from the rose extract, R-AuNPs, 4-MBA, and 4-MBA-coated R-AuNPs is given in the SI section (Table S1). Aromatic ligands used in this study have been categorized into two groups: (a) ligands with a thiol (−SH) headgroup, benzene ring as a linker, and acid (−COOH), amine (−NH$_3^+$),
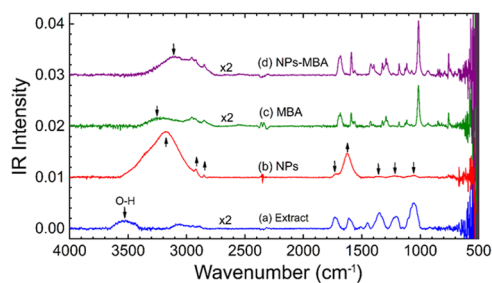

Figure 2. (a) Rose extract, (b) R-AuNPs, (c) 4-MBA solution of 0.9 × 10^{-3} M, (d) R-AuNP (20 μL) solution mixed with 4-MBA (180 μL of 10^{-3} M).
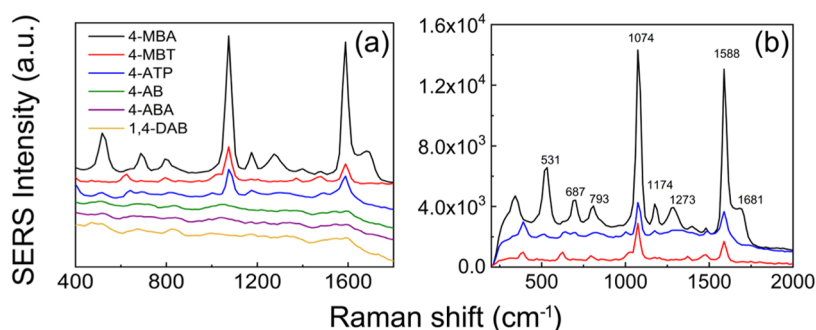
Figure 3. (a) SERS spectra of different ligands with a concentration of 1 mM on R-AuNPs. SERS spectra of different ligands on surface-catalyzed R-AuNPs. From top to bottom, the ligand sequence was 4-mercaptobenzoic acid (4-MBA), 4-methylbenzenethiol (4-MBT), 4-aminothiophenol (4-ATP), 4-aminobenzamide (4-AB), 4-aminobenzoic acid (4-ABA), and 1,4-diaaminobenzene (1,4-DAB). (b) SERS spectra of 4-MBA, 4-ATP, and 4-MBT with their specific vibrational bands.

or methyl group ($-CH_3$) as a tail group and (b) ligand with an amine ($-NH_2$) headgroup, benzene ring as a linker, and acid ($-COOH$), amide ($-CONH_2$), or amine group ($-NH_2$) as a tail group. Due to the strong affinity of the $-SH$ group toward surface gold atoms of R-AuNPs (covalent Au$-$S bond strength: 48 kcal mol^{-1}),[59] 4-MBA, 4-ATP, and 4-MBT, all are strongly attached to the surface of R-AuNPs and the tail groups are projected vertically outward (normal) with respect to the R-AuNP-surface. On the contrary, the Au$-$N coordinative bond has a higher electrostatic than covalent character, making 4-AB, 4-ABA, and 1,4-DAB adsorb loosely onto the surface of R-AuNPs, and the tail groups are not projected vertically outward with respect to the R-AuNP-surface.

This difference in geometry of the interaction for ligands with the surface of R-AuNPs results in enhanced Raman signals from the first group, while the second group does not show any Raman signal, as shown in Figure 3. Due to the strong covalent binding with the nanosurface, the first group of ligands remains close to the nanosurface to experience a strong near-field effect (one of the factors for SERS) and results in an intense SERS signal, whereas due to electrostatic binding, the second group of ligands remains apart from the nanosurface, not experiencing a strong near-field effect, and results in a weak or almost no SERS signal. Further, out of the first group ligands, 4-MBA shows a much higher SERS signal compared to 4-ATP and 4-MBT. Additionally, an extensive DFT study investigates the binding of selected molecules (4-MBA, 4-MBT, 4-ATP, 4-AB, 4-ABA, and 1,4-DAB) with Au(0)-thiol and Au(1)-thiolate clusters to understand their interactions with AuNPs, focusing on the behavior of Au(0)-thiol and Au(1)-thiolate compounds. It examines the formation of intermolecular and intramolecular hydrogen bonds between 4-MBA molecules interacting with Au_{10} clusters via sulfur atoms. The effect of inter- and intramolecular H-bonds on the structural and electrical characteristics of 4-MBA under varying electric fields (0 to 0.26 V Å^{-1}) is specifically evaluated. Figure 4 presents the ligand molecules and their bond lengths (S$-$Au) with Au_{10} clusters, highlighting that Au(1)-thiolate compounds have shorter S$-$Au bonds and additional stacking interactions compared with Au(0)-thiol compounds. These factors result in higher binding adsorption energies for 4-MBA@Au_{10}, 4-MBT@Au_{10}, and 4-ATP@Au_{10} in the Au(1)-thiolate configuration. Figure S3 shows the HOMO and LUMO levels for these ligands with Au_{10} clusters. The HOMO value for Au_{10} is -6.01 eV and the LUMO value for 4-MBA is -1.38 eV,

yielding a smaller energy gap of 4.63 eV, indicating significant electron transfer between Au and the ligand molecules. To explain this observation, we have theoretically calculated the charge transfer (CT) probability by estimating the energy gap between the LUMO$-$HOMO molecular orbital pair for 4-MBA@Au_{10} and the 4-MBA@$Au_{10}-$4-MBA@Au_{10} system. Moreover, the energy gaps between the LUMO and HOMO for the above two systems change by 7 and 27% when an electric field of 0.26 V Å^{-1} is applied. By considering a simple model of polarized light with the $\vec{E}$ vector along the interparticle axis for the 4-MBA@R-AuNP$-$4-MBA@R-AuNP can result in a charge separation between two R-AuNPs when they are coupled by an intermolecular hydrogen bond between surface-adsorbed 4-MBAs. Recently, Xu and Kall[60] and Xu et al.[61] have shown that when two nanoparticles are brought close together, the optical field strength in the interstice between the two particles can be increased so greatly that SERS enhancements of $\sim10^{11}$ can be obtained for molecules residing at that spot, provided that the two nanoparticles are brought close enough together (i.e., <1 nm), light of the appropriate wavelength is used, and the exciting electric field vector is polarized along the interparticle axis.

From our theoretical calculation, we found that the gap between two R-AuNPs when they remain connected through intermolecular hydrogen bonding between two 4-MBA is ~1.0 nm, making the situation suitable to generate a capacitor geometry and the generated coherent capacitive field sensed by the 4-MBA dimer. The dipole induced in each nano-object arises from the combined field of the incident light and the intense field of its partner, which, in this configuration, leads to an amplification of the polarization. If this problem is solved naively as one of the simple electrostatics involving two polarizable nanoparticles with a ζ-potential of -43.1 mV (here, the size of an individual R-AuNP is less than 1/10th of the excitation wavelength, and hence, contribution comes only from the dipolar polarization), then, light polarized along the interparticle axis can induce a capacitor just like a parallel plate capacitor. A point to be noted is that in our experiment, we used unpolarized light, light with random and time-varying polarization, and coupled nanoparticle systems are free to rotate in the solution. Hence, in an ensemble of molecular systems, the number of intermolecular hydrogen-bonded nanoparticle systems with the interparticle axis remaining parallel to the incident electric field vector ($\vec{E}$) is constant. The electric field strength in a capacitor is directly proportional to
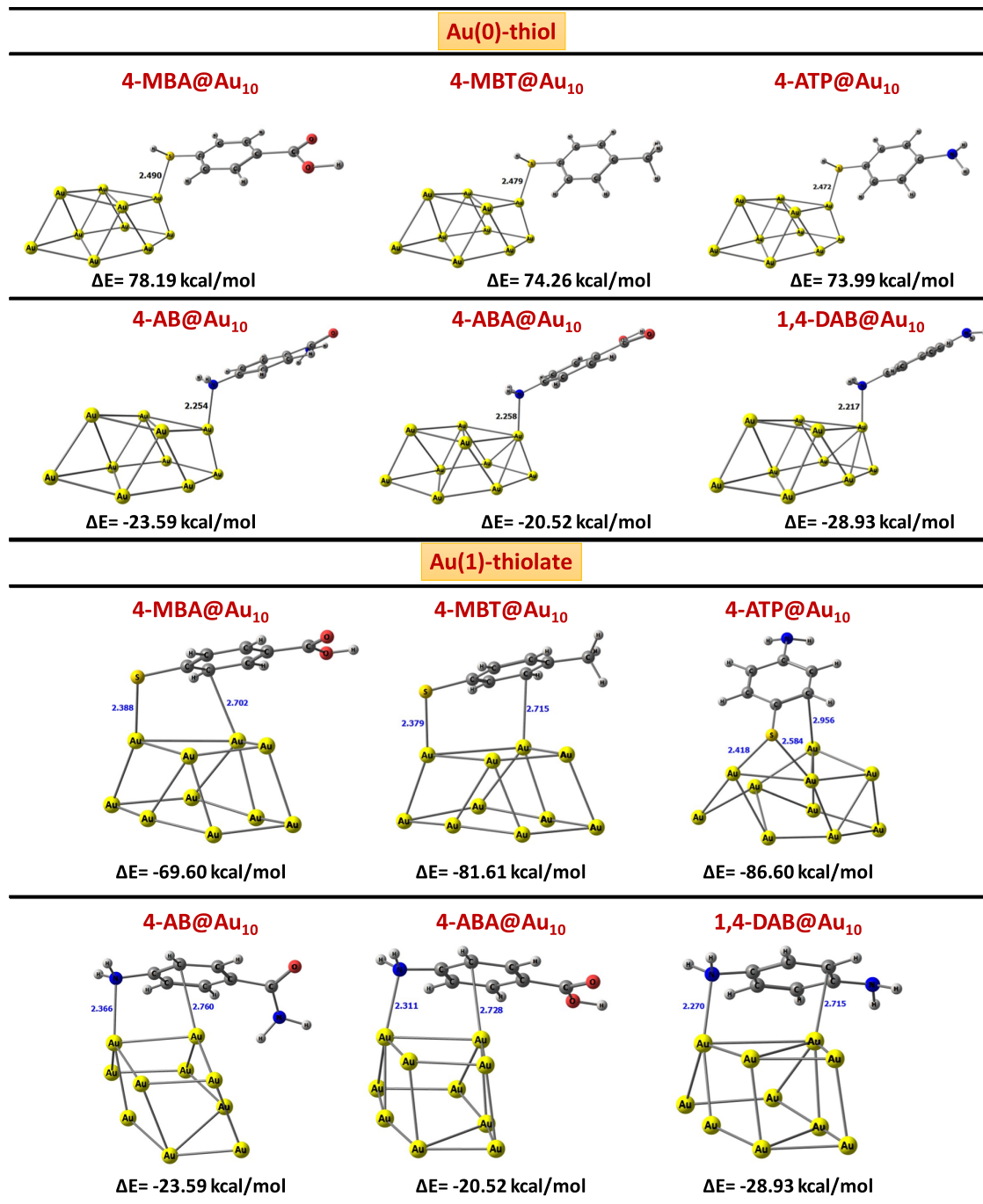
Au(0)-thiol

4-MBA@Au₁₀

4-MBT@Au₁₀

4-ATP@Au₁₀

ΔE= 78.19 kcal/mol   ΔE= 74.26 kcal/mol   ΔE= 73.99 kcal/mol

4-AB@Au₁₀

4-ABA@Au₁₀

1,4-DAB@Au₁₀

ΔE= -23.59 kcal/mol   ΔE= -20.52 kcal/mol   ΔE= -28.93 kcal/mol

Au(1)-thiolate

4-MBA@Au₁₀

4-MBT@Au₁₀

4-ATP@Au₁₀

ΔE= -69.60 kcal/mol   ΔE= -81.61 kcal/mol   ΔE= -86.60 kcal/mol

4-AB@Au₁₀

4-ABA@Au₁₀

1,4-DAB@Au₁₀

ΔE= -23.59 kcal/mol   ΔE= -20.52 kcal/mol   ΔE= -28.93 kcal/mol

Figure 4. Selected ligand molecules with Au(0)-thiol and Au(1)-thiolate clusters: selected S−Au bond lengths (Å), other possible stacking interaction distances (Å) within Au(1)-thiolate, and energy adsorption configurations (ΔE) in kcal/mol.

the voltage applied and is inversely proportional to the distance between the plates. This leads to the generation of a capacitive field, $E = \frac{V}{d} = \frac{43.1 \text{ mV}}{10^{-9} \text{ m}} = 4.3 \times 10^{7} \text{ V m}^{-1}$, for two R-AuNPs coupled by intermolecular hydrogen bonding with a separation of ~1 nm, and the field strength increases with decreasing distance between R-AuNPs. An idea about the adopted model is explained by Moscovits in his 2005 published *J. Raman Spectrosc.* paper. The adopted model in this study can be understood from Scheme 1.

Referring to Scheme 1a, the top panel explains how 4-MBA remains attached to the surface of an R-AuNP surface through a Au−S covalent bond, followed by intermolecular hydrogen

bonding between two R-AuNPs. The dimer of 4-MBA (indicated by a small solid dot in the figure) is located in the interstice between two metal nanospheres. Now, if we excite this system by an unpolarized light, a constant portion of the electric field vectors of the propagating light always remain in line with the free tumbled interparticle axis (by considering the speed of the electromagnetic wave propagation much higher than the external (translations) and internal (rotations and vibrations) motion of the 4-MBA@R-AuNP−4-MBA@R-AuNP system), and the crest (trough) of the electric field will repel (attract) free electrons from the first nanoparticle surface to polarize the nanoparticle in such a way that the approaching

Scheme 1. (a) (Top) Demonstration of the Formation of the 4-MBA@R-AuNP−4-MBA@R-AuNP System through the Intermolecular System, (Middle) Electromagnetic Polarization by an Unpolarized Light where the Electric Field Vector is Parallel to the Interparticle Axis, and (Bottom) Formation and Time-Varying Fluctuation of the Resultant Parallel Plate Capacitor and (b) (Top) Demonstration of the Formation of Individual 4-MBA@R-AuNP Systems, (Middle) Electromagnetic Polarization by an Unpolarized Light, and (Bottom) Formation of the Resultant Unstable Parallel Plate Capacitor
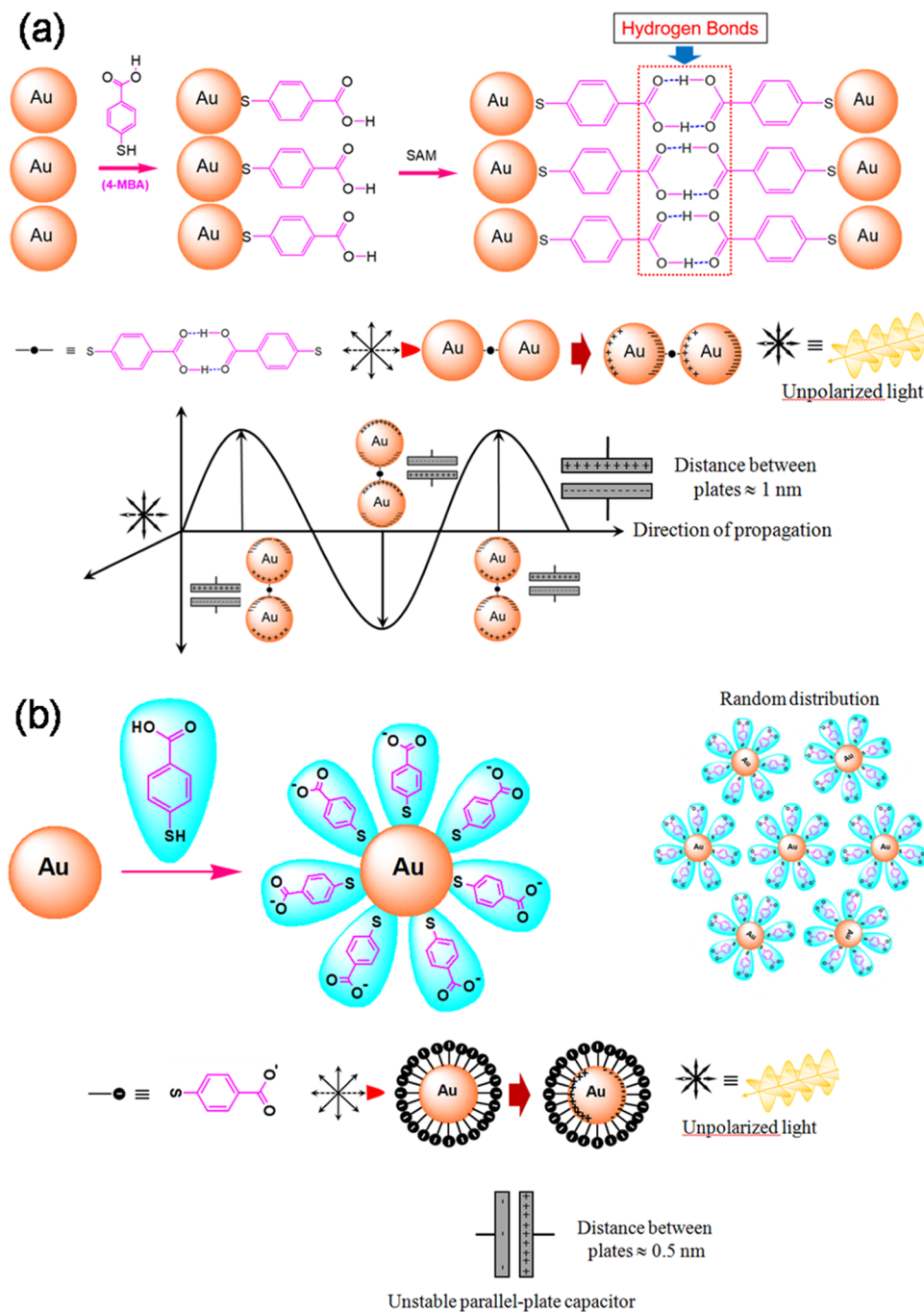
end became positively (negatively) charged and the rearing end became negatively (positively) charged. Since the second R-AuNP is attached to the first R-AuNP and remains in close proximity, intense polarization of the first R-AuNP induces polarization to the second R-AuNP (the approaching end became positively (negatively) charged and the rearing end became negatively (positively) charged). This results in an interconnecting nanoparticle system with two oppositely charged (negative (positive) for the first R-AuNP and positive (negative) for the second R-AuNP) parallel (on the nanoscale)

surfaces with a gap of ∼1 nm. The combined field of the incident light and the intense field of its partner, in this configuration, lead to an amplification of the polarization. Here, the dimer of 4-MBA is flanked by two sets of (time-varying) conjugate charges arising from the polarization of the individual nanoparticles. Since the distance between two nanoparticles is determined here by the intermolecular hydrogen bonding, the nanogap for this 4-MBA@R-AuNP− 4-MBA@R-AuNP system remains constant. This orientation of charge simply represents a case of a parallel plate capacitor

with a capacitive field in the range of 10^7 V m^{-1} as mentioned before. At such a high electric field, the interstice 4-MBA dimer modulates their HOMO−LUMO gap not by modulating their MLCT probability (as the case for 4-MBA@Au$_{10}$) but purely by the capacitive field as evident from our theoretical frontier molecular orbital (FMO) analysis. It is worth mentioning that a larger energy gap between the HOMO and LOMO for the 4-MBA@Au$_{10}$ system confirms the presence of thiolate bonding of 4-MBA with R-AuNP in the 4-MBA@R-AuNP−4-MBA@R-AuNP system. Out of the six different ligands we selected, only 4-MBA and 4-ABA can form intermolecular hydrogen bonding. A hard acid−soft base (HSAB) theory-based mechanism of intermolecular hydrogen bond formation is illustrated in detail in the SI section. As mentioned before, since 4-MBA remains covalently attached to the nanoparticle, the dimer of 4-MBA can suitably place itself in the interstice nanogap between R-AuNPs. On the contrary, since 4-ABA remains attached to the R-AuNP through electrostatic interactions, a dimer of 4-ABA forces them to detach from their respective nanoparticle and cannot place the dimer in the interstice nanogap between R-AuNPs to experience the capacitive force. Since the SERS intensity (I_{SERS}) relates linearly with the fourth power of the local field,[12] the gigantic local capacitive field in the above-described geometry enhances the SERS signal tremendously, which exceeds that at isolated metal particles by about 6 orders of magnitude.

Oppositely, if the electric field of the propagating light accidentally matches orthogonally with the interparticle axis, coupled (through intermolecular hydrogen bonding) nanoparticles will also show a time-varying polarization, but that does not represent a charge separation of a parallel plate capacitor configuration with respect to the interstice 4-MBA dimer as shown in Scheme S3. As a result of this, the interstice 4-MBA dimer does not experience the gigantic local capacitive field it experiences in the case of in-line (parallel) orientation; the SERS signal enhancement is almost negligibly different from its value at a single, isolated particle.

As explained before, due to the strong affinity of the −SH group toward surface gold atoms of R-AuNPs, 4-MBA, 4-ATP, and 4-MBT all are strongly attached to the surface of R-AuNPs and the tail groups are projected vertically outward (normal) with respect to the NP surface. Out of these three ligands, 4-MBA specifically makes a layer of negative charge on the nanoparticle surface with a distance of 0.5 nm between the R-AuNP surface and the negative charge layer, if we consider that there is no dimerization of 4-MBA between nearby R-AuNPs. In this situation, 4-MBA-coated R-AuNPs remain as individual nanoparticles. Now if we consider an unpolarized electromagnetic field-induced polarization for these individual nanoparticles, the crest (trough) of the electric field will repel (attract) free electrons from the nanoparticle surface to polarize the nanoparticle in such a way that the approaching end becomes positively (negatively) charged and the rearing end becomes negatively (positively) charged. In such a situation, a fluctuating crest (trough) will make a parallel plate capacitor in the approaching end (rearing end) with a distance of 0.5 nm between the plates. Unfortunately, the charge density on R-AuNP and surface ligands, in both the approaching and rearing ends, is not the same as argued in the following discussion.

Considering a close packing (without much interatomic gap) of Au atoms (with radius, $r = 0.144$ nm) in a 22 nm R-AuNP (radius, $R = 11$ nm), the number of Au atoms that can be accommodated in a single R-AuNP can be expressed as

$$N_1 = \frac{\text{volume of a single R-AuNP}}{\text{volume of a single Au atom}} = \frac{\frac{4}{3}\pi R^3}{\frac{4}{3}\pi r^3} = \left(\frac{R}{r}\right)^3$$

$$= \left(\frac{11}{0.144}\right)^3 = 445\,749$$

During the electromagnetic interaction with the R-AuNP, all 445,749 atoms will be collectively polarized to construct one of the plates of a parallel plate capacitor.

Considering the same close packing of Au atoms, the number of surface Au atoms available for ligand binding can be calculated as

$$N_2 = \frac{\text{total surface area of a single R-AuNP}}{\text{exposed surface area of a single Au atom}} = \frac{4\pi R^2}{2\pi r^2}$$

$$= 2\left(\frac{R}{r}\right)^2 = 2\left(\frac{11}{0.144}\right)^2 = 11\,670$$

Therefore, only 11,670 Au atoms will be available to bind an equal number of 4-MBA. If we consider that half of them are attached in the front face with the remaining half attached on the rear face, the total number of negative charge contributions from ligands toward the parallel plate capacitor is only 5835. This huge difference in charge polarization between Au (number of contributing Au atoms: 445,749) and 4-MBA (number of contributing 4-MBA: 5835), more than 75 times, makes the parallel plate capacitor very unstable, and hence, it may not contribute effectively to enhance the induced electromagnetic field suitable for the enhancement of the resultant Raman cross-section of the surface-adsorbed ligand, like 4-MBA. Conceptually, the development of a single-particle parallel capacitor is described in Scheme 1b.

Raman spectra of 4-MBA typically exhibit distinctive peaks corresponding to vibrational modes of the molecule, i.e., −O−H stretching at ∼3251 cm^{-1} (w), −C−H stretching at 2957.1 to 2848.1 cm^{-1} (w), −S−H stretching at 2558.7 cm^{-1} (w), >C=O stretching at 1685.4 cm^{-1} (s), −C−C(OOH) stretching at 1591.2 cm^{-1} (s), C−C stretching at 1562 cm^{-1} (w), various (C−COOH, C−H, O−H, etc) in-plane bending in the range of 1425−1281.6 cm^{-1} (w), a contribution from combined C−C and C−S stretching at 1016.3 cm^{-1}, and −S−H bending at 848.3 cm^{-1}. When the Raman signal of 4-MBA is monitored in the presence of R-AuNPs, we get a gigantic Raman signal enhancement. Like Raman spectroscopy, we also observe an enhancement in IR absorption when we record the vibrational spectra of 4-MBA on the R-AuNP surface. Interestingly, both IR and SERS show few common enhanced peaks, which include SERS$_{C-S}$ at 1074 and 1017 cm^{-1}, SERS$_{(C-C)str}$ at 1588 cm^{-1}, and SERS$_{(C=O)str}$ at 1681 cm^{-1}. Information about a few other strong SERS peaks at 531, 687, 793, and 1273 is not able to be extracted from ATR FT-IR spectra either due to the bandpass filter or low-vibrational cross-section. The calculation of the SERS enhancement factor (EF) for 4-MBA on R-AuNPs is elaborated in detail in the SI section. Here, we have calculated N_{bulk} and N_{SERS} separately and from the experimentally measured values of I_{bulk} and I_{SERS}, we have estimated the enhancement factor (EF). Experimentally obtained enhanced Raman spectra (on the R-AuNP surface) in comparison to the bulk Raman for 4-MBA are shown in Figure S4. Table S2 lists different parameters for
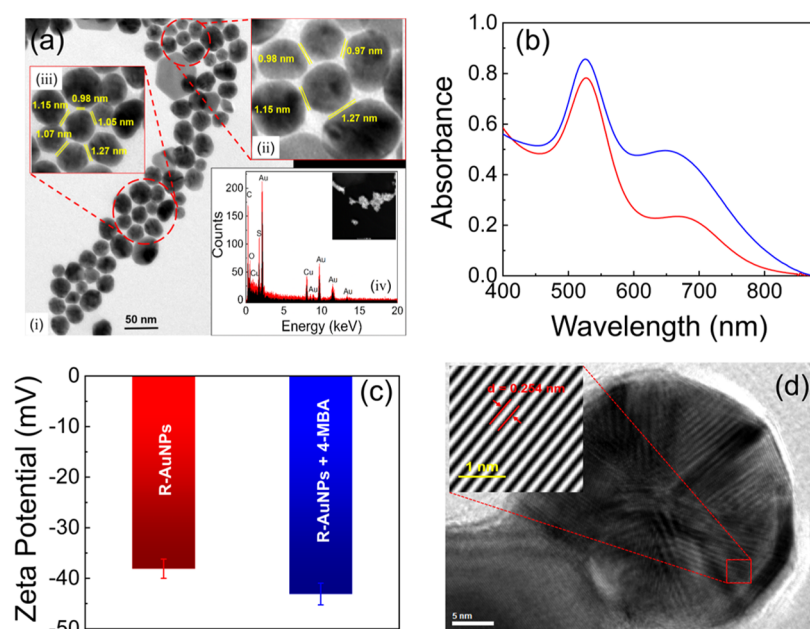
Figure 5. (a)[(i−iii)] Ordered arrangement of R-AuNPs after surface binding with 4-MBA and (a)[iv] EDX analysis of R-AuNPs after surface binding with 4-MBA. An intense peak at 1.9 keV proves the presence of sulfur (S) in the 4-MBA-R-AuNP adduct, (b) plasmon characteristics of R-AuNPs before (red line) and after binding (blue line) with 4-MBA, (c) variation of ζ-potential as a result of 4-MBA binding on the R-AuNP surface, and (d) variation of crystallization as a result of 4-MBA binding on the R-AuNP surface.

calculating the EF and estimates an enhancement factor of 6.88 × 10⁷ for the 1074 cm⁻¹ Raman band for C−S stretching. By considering the average diameter of R-AuNPs as 22 nm, comparing the intensity of the 1074 cm⁻¹ peak (C−S stretching vibration) for bulk and surface-adsorbed 4-MBA estimates an EF of 6.88×10^7. Compared to the capacitive field mechanism for SERS enhancement, in this work, the literature is rich in reporting the formation of hot spots in enhancing the SERS intensity to the same extent as we described for the capacitor model. Moreover, there is strong evidence that the theoretical SERS enhancement values for 4-MBA, 4-MBA@ Au_{10}, and 4-MBA@Au_{10}−4-MBA@Au_{10} molecules are in close agreement with the experimental data (in terms of frequency shifting and intensity change), as demonstrated by the computed IR and Raman activities and listed in Table S3.

Traditionally, hot spots are initiated by a three-dimensional (3D) electrostatic interaction between a Raman-active molecule and nanoparticles and ultimately result in an aggregation when there is almost zero spatial gap between nanoparticles with an interstitial Raman tag. Since the gap between nanoparticles in a hot spot is not controlled by molecular assembly, the possibility of aggregation increases with time, which results in an unstable SERS signal. This is not a problem for the described nanoassembly, which does not result in aggregation. Recorded TEM images (Figure 5ai−iii) of R-AuNPs after binding with 4-MBA show some sort of ordered arrangement of nanoparticles (NPs are displayed in the adduct form, i.e., like touching closely), which directly proves the subsequent inter/intramolecular hydrogen bonding. From EDAX analysis, an intense peak at 1.9 keV (Figure 5aiv) proves the presence of sulfur (S) in the 4-MBA@R-AuNP adduct, which also suggests the presence of Au−S as we have confirmed from the ATR FT-IR spectra. Bringing two nanoparticles closer than 1 nm initiates other effects, which include effective plasmon coupling where the original plasmon resonance splits into two polarization-sensitive components,

one of which (at a higher wavelength) has a resonance that depends strongly on the separation between R-AuNPs. Since in our case, R-AuNPs are coupled through an intermolecular hydrogen bond with an effective separation, $d \geq 1$ nm, we do not observe any plasmon coupling and the plasmon characteristics remain unchanged before and after binding with 4-MBA as shown in Figure 5b. Due to the presence of an acid group in neutral pH, the binding of 4-MBA on R-AuNPs increases the effective ζ-potential of assembled nanoparticles, as shown in Figure 5c. Since this intermolecular hydrogen bonding does not effectively affect the crystallization of individual R-AuNPs, their crystalline nature remains unchanged as shown in Figure 5d. Hence, this 4-MBA-induced stabilization not only brings nanoparticles close to each other but also allows Raman-active molecules to remain in close proximity to the metal surface for a longer duration without making any aggregation, increasing the probability of Raman scattering events. Additionally, the intermolecular H-bonding can modulate the enhanced local electromagnetic field (E_s) by altering the geometry of the nanoparticle assembly. With the generated enhanced local electromagnetic field (E_s) as a result of the formation of the parallel plate capacitor, the interstitial (hydrogen-bonded) 4-MBA molecules experience the same enhanced field and thus affect the EM enhancement mechanism. Again, due to the chemical interaction of 4-MBA with the nanoparticle surface and making effective intermolecular hydrogen bonding to bridge two R-AuNPs, the resultant polarizability (α_R) of the scatterer (4-MBA) will include contributions from the metals and may, as a result, be greatly altered in its magnitude, symmetry, and resonant properties from the polarizability of the isolated molecule (α_{R_0}).

Alteration of polarizability and thereby contribution toward the enhancement of the Raman scattering cross-section estimate the contribution through the CM mechanism. A detailed mathematical calculation by Avouris and Demuth[11,62]
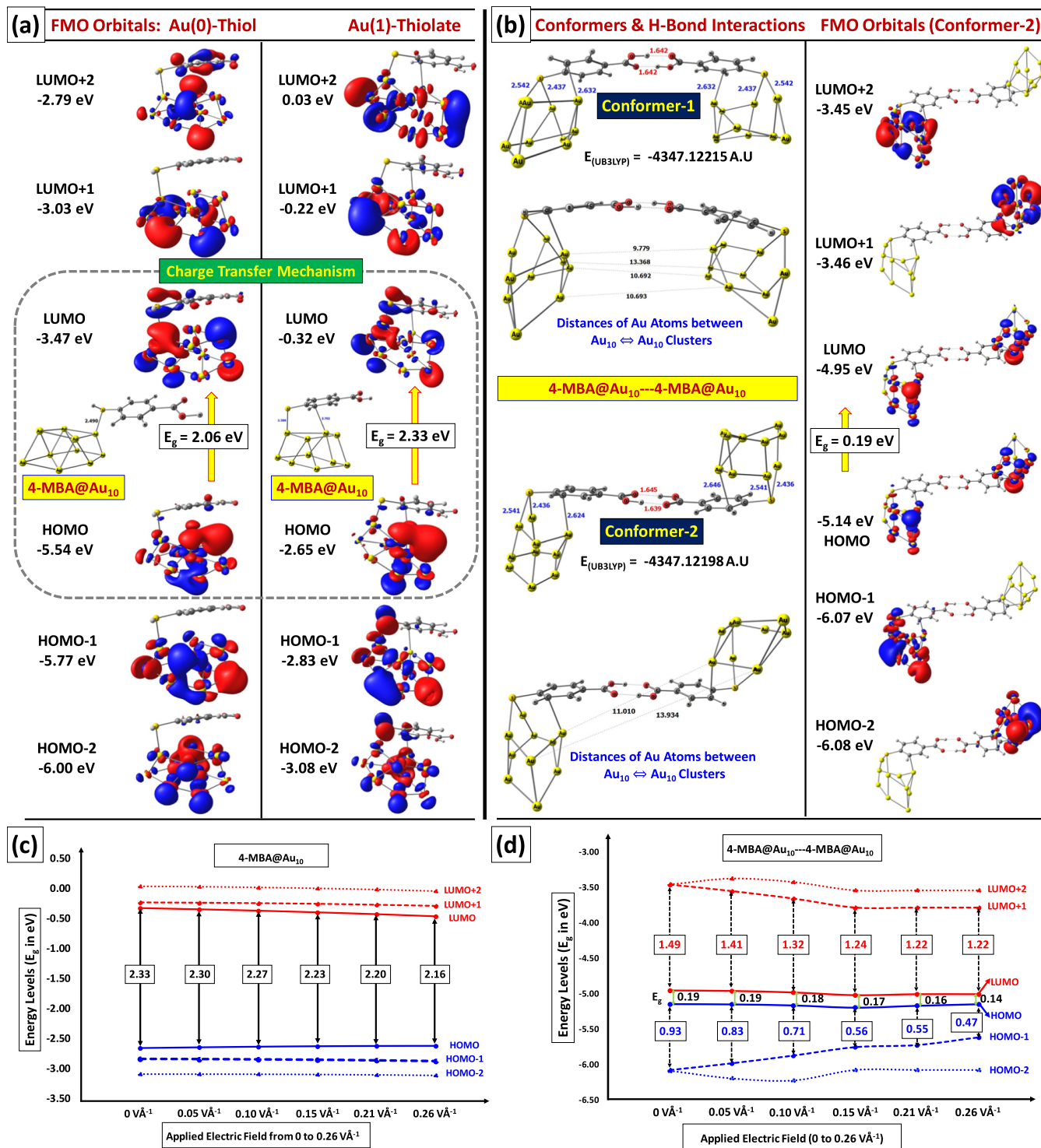
Figure 6. (a) Frontier molecular orbitals and their corresponding HOMO − 2 to LUMO + 2 values of 4-MBA with Au(0)-thiol and Au(1)-thiolate clusters. (b) Stability of optimized geometries, potential conformers, and their intercluster distances (in Å), including the FMO depicting the HOMO to LUMO levels. (c) HOMO−LUMO energy gap values of 4-MBA@Au$_{10}$ within the Au(1)-thiolate clusters with an applied electric field range of 0−0.26 V Å^{-1}. (d) HOMO−LUMO energy gap values of 4-MBA@Au$_{10}$−4-MBA@Au$_{10}$ in Au (1)-thiolate clusters with an applied electric field range of 0−0.26 V Å^{-1}.

estimates a chemical enhancement, $\eta_{chem} \approx 30 \left| \frac{d^2}{\alpha_R} \right|^2$, which yields enhancements in the range of 10−100 for typical ratios of $\frac{d^2}{\alpha_R}$, where "d" is the distance between the molecule and the metal surface and α_R is the polarizability of specific Raman

modes. Since "d" is constant (by intermolecular H-bonding) in our case, we can expect a larger enhancement for modes having lower polarizabilities. In general, the CM mechanism comes into play when there is an effective charge transfer between the metal and the surface-adsorbed/attached ligand. As a result of this metal−ligand charge transfer, the modified HOMO−
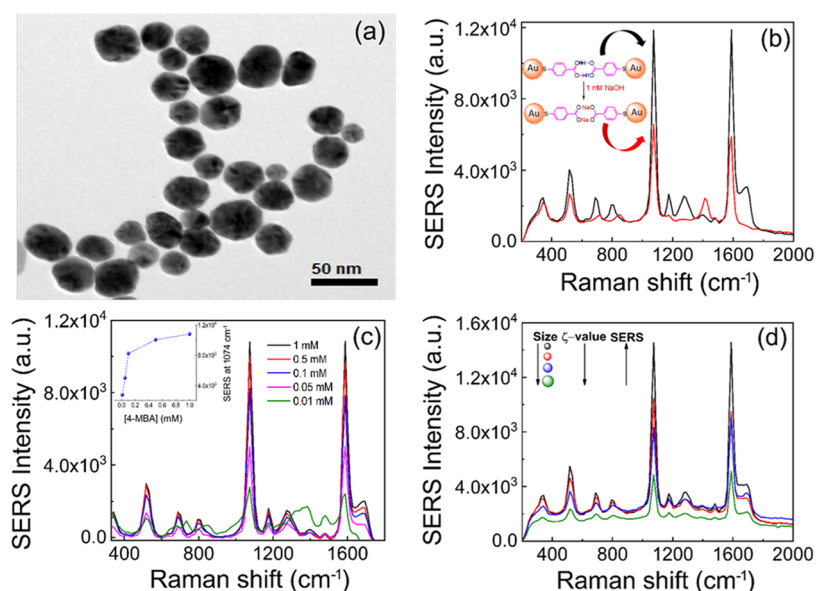
Figure 7. (a) Disruption of intermolecular H-bonding as a result of the addition of NaOH into the 4-MBA@R-AuNP−4-MBA@R-AuNP adduct, (b) diminished SERS intensity as a result of the disruption of H-bonding between 4-MBA adsorbed on two different R-AuNPs, (c) linear variation of SERS intensity originating from 4-MBA as a function of the concentration of surface-adsorbed 4-MBA (between 1 and 0.01 mM), and (d) variation of ζ-potential and SERS activity as a result of size variation.

LUMO transition finds resonance or near resonance with the excitation photon, while the HOMO−LUMO transition in the free molecule may be too energetic to excite with the same excitation source. Free 4-MBA shows a HOMO−LUMO transition at 4.54 eV (273 nm). When 4-MBA remains attached to a single R-AuNP and makes a monolayer without making any intermolecular hydrogen bonding, our theoretical calculation shows a prominent charge transfer between the metal and ligand in the case of HOMO−LUMO transition both in Au(0)-thiol and Au(1)-thiolate complexes with a substantial reduction in the HOMO−LUMO gap compared to the free 4-MBA as shown in Figure 6a. Also, a high HOMO−LUMO gap (2.33 eV) gradually reduces minimally (∼7%) as we increase the operating unstable capacitive field between the metal surface (serves as the anode) and the SAM charge, as shown in Figure 6c. The resultant HOMO−LUMO gap at a higher capacitive field for the 4-MBA@Au$_{10}$ system is calculated as 2.16 eV, which is again close to our excitation source (1.85 eV) for the Raman experiment. On the contrary, when 4-MBA molecules remain in intermolecular hydrogen-bonded conditions between two R-AuNPs, there is no observable metal-to-ligand charge transfer in the case of HOMO−LUMO transition as shown in Figure 6b. Also, a very low HOMO−LUMO gap (0.19 eV) further reduces (∼27%) as we increase the operating capacitive field between the metal surface and SAM charge, as shown in Figure 6d. Hence, our theoretical calculation shows that the high SERS activity in our case where 4-MBA remains in the intermolecular H-bonding state has a minimal role from charge transfer contribution and the observed Raman enhancement can solely be explained by the EM mechanism. Although in the present case, the estimation of the relative weightage of the enhancement factors is easy, in most cases where both EM and CM mechanisms contribute toward SERS enhancement, the accurate estimation of their relative weightage is not an easy task. In general, the contribution of EM is 4−8 orders more than CM to enhance the surface-enhanced Raman scattering.

Moreover, once the nanoparticles are assembled due to intermolecular hydrogen bonding between 4-MBA molecules, the system almost remains unaffected by any sort of chemical influence from nanoparticles. Hence, the chemisorption of the 4-MBA molecule on the R-AuNP leads to the formation of a stable intermolecular H-bonding to offer a larger SERS intensity with a high enhancement factor (EF ∼ 10^7) originating mostly from the electromagnetic field enhancement. To prove the impressive role of intermolecular H-bonding in enhancing the SERS signal, we introduced sodium ions (Na$^+$) into the 4-MBA@R-AuNP−4-MBA@R-AuNP adduct by adding an equivalent amount of NaOH to 4-MBA.

The high ionic strength of NaOH disrupts intermolecular H-bonding interactions between carboxylate groups (−COOH) of 4-MBA by screening the charges and reducing the effective attraction between molecules. Disruption of intermolecular H-bonding results in individual R-AuNPs with 4-mercapto sodium benzoate absorbed onto the nanosurface. A reduced ordering of R-AuNPs compared to Figure 5a with a diminished SERS intensity, shown in Figure 7a,b, proves the merit of our proposed model. A systematic record of the depletion of the SERS intensity with NaOH can effectively measure the concentration of sodium ions in an unknown solution. The incapability of intermolecular H-bond formation for two other thiolated aromatic compounds with almost similar dimensions, 4-ATP and 4-MBT, cannot support the coherent capacitor model and results in a much weaker SERS intensity compared to the one offered by 4-MBA. Moreover, the recorded SERS intensity (a histogram plot of SERS intensity at 1074 cm^{-1} vs [4-MBA]) linearly varies with the concentration of 4-MBA, which shows a measurable SERS signal at 10^{-5} M and maximizes at 10^{-3} M as shown in Figure 7c.

Considering the formation of a capacitor due to the optical polarization of an H-bonded coupled system with a magnitude of charge on the inner faces of connected nanoparticles as Q, capacitance of the generated capacitor as C, and generated potential difference between the particles as V, we can express
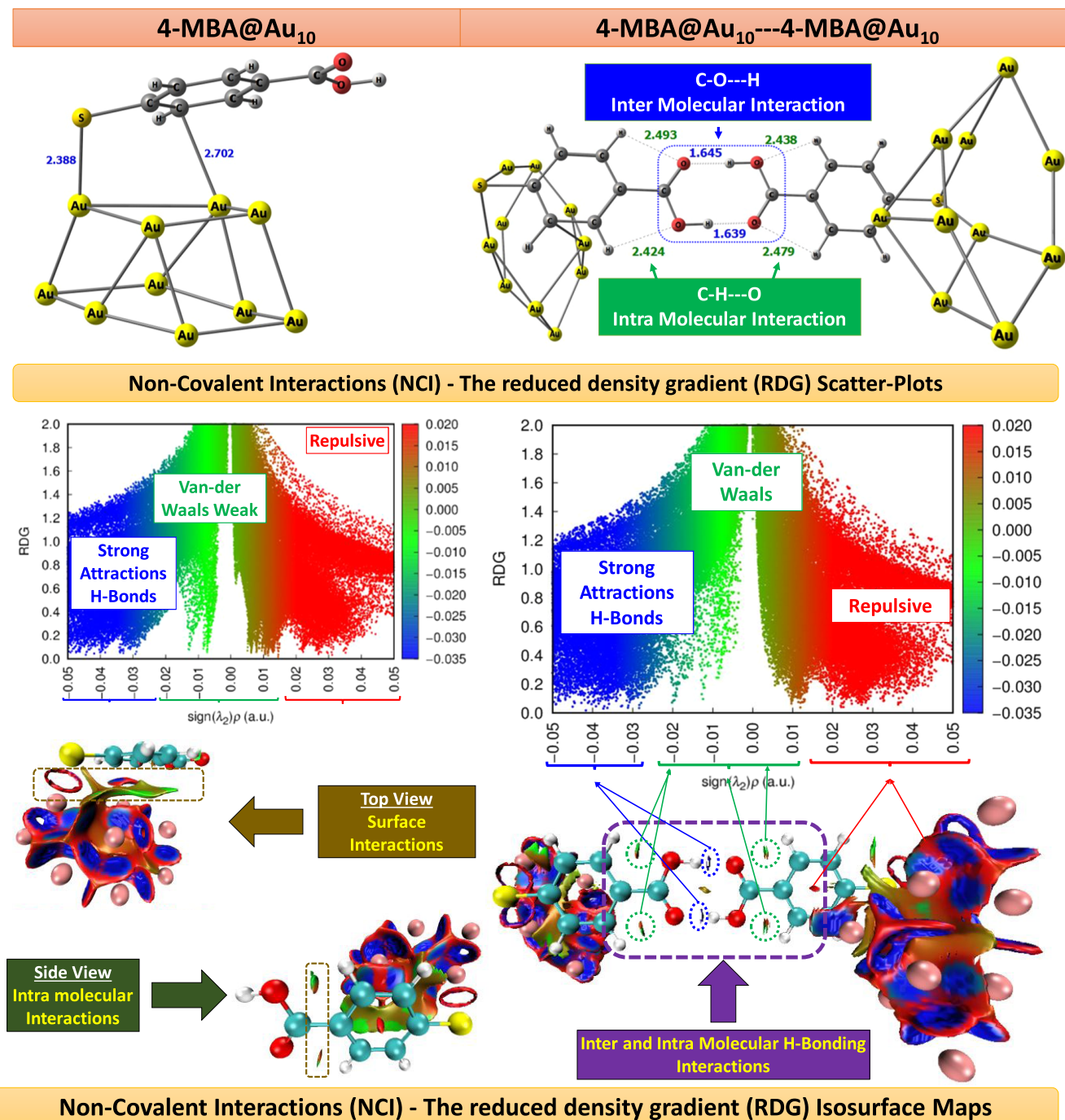
Figure 8. Computed RDG isosurfaces for 4-MBA@Au10 and 4-MBA@Au$_{10}$−4-MBA@Au$_{10}$ from NCI analysis. The isosurfaces correspond to an isovalue of 0.5 au and a color scale of $0.1 < \rho < 0.1$.

$Q = \text{CV}$ or $V = \frac{Q}{C} = \frac{Q}{A\varepsilon_0 / d} = \frac{Qd}{A\varepsilon_0}$, where "$A$" is the area of the polarization of the nanoparticle surface, "ε_0" is the permittivity of the media, and "d" is the separation between R-AuNPs. Since the generated field can be expressed mathematically as $E = \frac{dV}{dR}$, where R is the distance (same as "d"), the generated capacitive field $E = \frac{d\left(\frac{Qd}{A\varepsilon_0}\right)}{dR} = \frac{Q}{A\varepsilon_0}$. Simply by varying the diameter of the synthesized R-AuNP, we can vary the surface charge (Q) as well as the area of the polarization of the nanoparticle surface (A) to control the effective capacitive field

(E). A gradual increment in size shows a gradual reduction of surface charge, as measured from their ζ-potential, with a gradual increment of "A", which shows a diminished SERS activity when we combine R-AuNPs through intermolecular H-bonding between surface-attached 4-MBAs. The obtained result is evident from Figures 7d and S5. To find out the effect of surface charge on the extent of SERS enhancement, along with R-AuNPs, we have also synthesized trisodium citrate (TSC)-based negatively charged spherical nanoparticles of an average diameter of 22 nm and hexadecyltrimethylammonium bromide (CTAB)-based positively charged spherical-shaped nanoparticles of an average diameter of 23 nm. Surprisingly,

both TSC- and CTAB-capped nanoparticles show very low SERS enhancement efficiency as shown in Figure S6. Moreover, both TSC- and CTAB-capped nanoparticles show a time-dependent aggregation (absorption spectra with a shifted plasmon band and the appearance of an additional plasmon peak at a higher wavelength due to aggregation), shown in Figure S7, which again leads to diminished SERS activity. As mentioned before, a multicomponent natural extract from rose petals molds the nanoparticle surface in such a way that the externally added Raman-active ligands (4-MBA) make a self-assembled monolayer on the nanoparticle either to remain as isolated particles or to make intermolecular hydrogen bonds between nearby nanoparticles without making any aggregation as compared to TSC- and CTAB-capped nanoparticle. A comparison of the SERS signal strength from R-AuNPs with TSC- and CTAB-capped AuNPs is shown in Figure S6.

To determine the influence of laser power on SERS signal intensity, we performed a power-dependent SERS study of the 4-MBA@R-AuNP−4-MBA@R-AuNP system by varying the laser power between 0.70 and 2.79 mW and recording the Raman signal strength at 1074 cm^{-1}. We can correlate the signal intensity with laser power by $S_n = KP^n$ or $\log(S_n) = n \times \log(P) + \log(K)$. Here, S_n indicates the signal intensity corresponding to the n-photon absorption and P is the laser power. The slope (=1.0) of the log−log plot between laser power and signal intensity indicates that the signal is linearly dependent on laser power, or in other words, the observed SERS is a single photon process, as shown in Figure S8. For the sake of argument, if we consider that there is no hydrogen bonding between R-AuNPs when 4-MBA is bonded on their surface, all R-AuNPs remain as individual nanoparticles in the presence of 4-MBA. In this condition, an electromagnetic excitation will polarize individual nanoparticles with two opposite layers of charges on opposite faces of the nanoparticle. This also makes a parallel plate capacitor geometry, but since the gap between the two charge layers is ∼22 nm (diameter of the particle), the experienced capacitive field $\left(E = \frac{V}{d}\right)$ is too small. Moreover, most of the surface-adsorbed molecules remain outside of this force field and hence cannot contribute to the enhancement of the SERS signal.

Numerically, we understood that with a decrease in distance, the effective capacitive field enhanced, and theoretically, we proved that an increment in the capacitive field influences the HOMO−LUMO gap of the adduct. As mentioned before, there is a finite HOMO−LUMO gap for the 4-MBA@Au$_{10}$ system (2.33 eV) in the absence of a capacitive field, which reduces (7%) to 2.16 eV under the application of a capacitive field of 0.26 V Å^{-1}. On the contrary, there is a negligibly small HOMO−LUMO gap for 4-MBA@Au$_{10}$−4-MBA@Au$_{10}$ system (0.19 eV) in the absence of a capacitive field, which reduces (27%) further to 0.14 eV under the application of a capacitive field of 0.26 V Å^{-1}. This clearly proves that our adopted capacitive model can easily account for the enhanced possibility of excitation for the observed SERS enhancement. Furthermore, Figure 8 examines the characteristics of 4-MBA@Au$_{10}$−4-MBA@Au$_{10}$, detailing H-bonding and stacking interactions on the Au$_{10}$ cluster surface and the distance between two Au$_{10}$ clusters. It presents two conformers along with their total energies, indicating molecular stability with a minimal energy difference of only 0.45 kJ/mol (as shown in Figure 6) between the two. In Conformer-2, H-bonding

interactions occur at 1.645 and 1.639 Å. Both conformers display similar stability and planarity on the 4-MBA ligand and the Au$_{10}$ surface. The 4-MBA ligands exhibit stronger H-bonding interactions than other ligands, supporting experimental findings. Overall, electromagnetic and chemical enhancement mechanisms serve as the main drivers of SERS enhancement. However, hydrogen bonding interactions have the potential to complement and amplify these effects, resulting in improved sensitivity and enhanced signals for molecular detection and analysis in SERS.

NCI analysis visualizes noncovalent interactions as attractive (blue), repulsive (red), and weak van der Waals (vdW) (green), as shown in Figure 8. The figure highlights weak van der Waals (vdW) interactions, stacking repulsions, and strong attractive H-bonds between the planar 4-MBA ligand and the Au$_{10}$ surface. The significant blue and green surfaces indicate robust interactions with the Au surface. The sulfur atom's negative charge dispersion and the planarity of 4-MBA improve the interaction with the Au surface. The optimization of 4-MBA relies on H-bonding interactions, enhancing the SERS mechanism and stabilizing the adsorbed 4-MBA molecules. The smaller energy gap for 4-MBA with Au$_{10}$ clusters, compared to those of other ligands, demonstrates effective charge transfer from Au$_{10}$ clusters to the sulfur atom of 4-MBA, as supported by the HOMO distribution and smaller HOMO−LUMO gap.

Our newly synthesized R-AuNP also shows good SERS activity with other common dye molecules such as crystal violet (CV),[63] Rhodamine 6G (Rh6G),[64] Rhodamine B (Rh−B),[65] and Congo Red (CR)[66] having good Raman cross-sections. SERS spectra and assignment of different bands obtained from different dyes are elaborated in the SI section (Figure S9 and Table S4). The absence of an S atom in all those dyes allows the positively (+ve) charged dye molecules to bind on the surface of negatively (−ve) charged R-AuNPs through an electrostatic interaction. As mentioned before, an uncontrolled electrostatic interaction leads to aggregation of nanoparticles with time. Hence, our synthesized R-AuNP is overall a good Raman substrate, but its potentiality as an outstanding SERS matrix can be explored by generating an intermolecular H-bonding-mediated nanoparticle assembly to create a gigantic capacitive field at the interstitial nanojunction.

4. CONCLUSIONS

Multicomponent natural rose petal extract as a surfactant helped us to mold the nanoparticle surface in such a way that the external addition of a thiolated aromatic compound (4-MBA, 4-ATP, and 4-MBT) makes a self-assembled monolayer on the nanoparticle either to remain as isolated particles (for 4-ATP and 4-MBT) or to make an intermolecular hydrogen bond between nearby nanoparticles (for 4-MBA) without making any aggregation. Formation of coupled R-AuNPs with interstitial H-bonding between surface-adsorbed 4-MBAs allowed us to generate parallel plate capacitors in the nanoscale upon electromagnetic excitation and the generated capacitive field (4.3×10^7 V m^{-1}) accounts efficiently for the observed enhancement factor of 6.88×10^7. Our theoretical calculation helps us to understand the interrelation among the distance between nanoparticles, the increased role of intermolecular H-bonding in molecular stabilization, and modulation of the HOMO−LUMO gap when we move from the 4-MBA@Au$_{10}$ system (2.33 eV) to the 4-MBA@Au$_{10}$−4-MBA@Au$_{10}$ system (0.19 eV), allowing us to formulate a coherent capacitive

coupling model to account for an enhanced Raman activity upon electromagnetic excitation. A comparison between the experimentally obtained SERS sensitivity and a DFT level theoretical calculation shows that the obtained high SERS activity in our case where 4-MBAs remain in the intermolecular H-bonding state has a minimal role from charge transfer contribution and the observed Raman enhancement can solely be explained by the EM mechanism. In the future, we plan to justify our model by considering anisotropic nanoparticles (rose petal-based) with sharp edges or tips to enhance the capacitive field for higher order Raman enhancement.

■ ASSOCIATED CONTENT

Ⓢ Supporting Information

The Supporting Information is available free of charge at https://pubs.acs.org/doi/10.1021/acsomega.4c05118.

> Schematic diagram for the synthesis of rose petal extract and gold nanoparticles; instrumentation; characterization of R-AuNPs; dependency of absorption bands of nanoparticles on their physical and chemical characteristics; SEM of the synthesized R-AuNPs; mechanism of SAM formation by 4-MBA on R-AuNPs; IR band assignment; FMO energy levels for possible charge transfer mechanisms in the Au(1)-thiolate nanosystem; mechanism of intermolecular hydrogen bond formation; time-varying polarization of propagating electromagnetic field where the electric field polarization is perpendicular to the interparticle axis; calculation of the SERS enhancement factor for 4-MBA; computed IR and Raman activity of 4-MBA, 4-MBA@Au$_{10}$; and 4-MBA@Au$_{10}$−4-MBA@Au$_{10}$ systems; relation between the size of the synthesized R-AuNP with surface charge and SERS activity; SERS spectra of 4-MBA on different nanosurfaces; aggregation behavior of different nanoparticles (R-AuNP, TSC-AuNP, and CTAB-AuNP) in the presence of 4-MBA; power-dependent SERS study; and assignment of different SERS bands obtained from different dyes by using R-AuNP as the SERS substrate (PDF)

■ AUTHOR INFORMATION

Corresponding Author

　　Dulal Senapati − *Chemical Sciences Division, Saha Institute of Nuclear Physics, A CI of Homi Bhabha National Institute, Kolkata 700064, India;* ⓞ orcid.org/0000-0001-5002-4631; Email: dulal.senapati@saha.ac.in

Authors

　　Amar Ghosh − *Biophysical Chemistry Laboratory, Physical Chemistry Section, Department of Chemistry, Jadavpur University, Kolkata 700032, India*

　　Murugesan Panneerselvam − *MolMod-CS—Instituto de Química, Universidade Federal Fluminense, 24020-14 Rio de Janeiro, Brazil*

　　Sourav Mondal − *Chemical Sciences Division, Saha Institute of Nuclear Physics, A CI of Homi Bhabha National Institute, Kolkata 700064, India*

　　Prasanta Das − *Department of Chemistry, Faculty of Sciences, Ganpat University, Mehsana 384012 Gujarat, India;* ⓞ orcid.org/0000-0003-1488-2991

　　Tukai Singha − *Surface Physics and Material Science Division, Saha Institute of Nuclear Physics, A CI of Homi Bhabha National Institute, Kolkata 700064, India*

　　Subhasis Rana − *Department of Basic Science and Humanities, Institute of Engineering and Management, University of Engineering and Management, Kolkata 700160, India*

　　Luciano T. Costa − *MolMod-CS—Instituto de Química, Universidade Federal Fluminense, 24020-14 Rio de Janeiro, Brazil;* ⓞ orcid.org/0000-0002-9967-4034

　　Biswarup Satpati − *Surface Physics and Material Science Division, Saha Institute of Nuclear Physics, A CI of Homi Bhabha National Institute, Kolkata 700064, India;* ⓞ orcid.org/0000-0003-1175-7562

　　Suman Das − *Biophysical Chemistry Laboratory, Physical Chemistry Section, Department of Chemistry, Jadavpur University, Kolkata 700032, India;* ⓞ orcid.org/0000-0002-4148-1002

　　Ujjal Kumar Sur − *Department of Chemistry, Behala College, Kolkata 700060 West Bengal, India*

Complete contact information is available at:
https://pubs.acs.org/10.1021/acsomega.4c05118

Notes

The authors declare no competing financial interest.

■ ACKNOWLEDGMENTS

■ REFERENCES

(1) Wang, Y.; Ji, W.; Sui, H.; Kitahama, Y.; Ruan, W.; Ozaki, Y.; Zhao, B. Exploring the effect of intermolecular H-bonding: a study on charge-transfer contribution to surface-enhanced Raman scattering of p-mercaptobenzoic acid. *J. Phys. Chem. C* **2014**, *118* (19), 10191−10197.

(2) Li, C.; Wu, C.; Zhang, K.; Chen, M.; Wang, Y.; Shi, J.; Tang, Z. The charge transfer effect on SERS in a gold-decorated surface defect anatase nanosheet/methylene blue (MB) system. *New J. Chem.* **2021**, *45* (42), 19775−19786.

(3) Dongming, L.; Shuhai, J.; Jun, W.; Yang, J. Ordered silver nanoparticle arrays as surface-enhanced Raman spectroscopy substrates for label-free detection of vitamin C in serum. *Sens. Actuators, A* **2013**, *201*, 416−420.

(4) Le Ru, E. C.; Etchegoin, P. G. *Principles of Surface-Enhanced Raman Spectroscopy and Related Plasmonic Effects*; Elsevier: Amsterdam, The Netherlands, 2009.

(5) Su, Y.; Shi, Y.; Wang, P.; Du, J.; Raschke, M. B.; Pang, L. Quantification and coupling of the electromagnetic and chemical contributions in surface-enhanced Raman scattering. *Beilstein J. Nanotechnol.* **2019**, *10* (1), 549−556.

(6) Zhang, Y.; Walkenfort, B.; Yoon, J. H.; Schlucker, S.; Xie, W. Gold and silver nanoparticle monomers are non-SERS-active: a negative experimental study with silica-encapsulated Raman-reporter-coated metal colloids. *Phys. Chem. Chem. Phys.* **2015**, *17* (33), 21120−21126.

(7) Fleischmann, M.; Hendra, P. J.; Mcquillan, A. J. Raman spectra of pyridine adsorbed at a silver electrode. *Chem. Phys. Lett.* **1974**, *26* (2), 163−166.

(8) Jeanmaire, D. L.; Van Duyne, R. P. Surface Raman spectroelectrochemistry: Part I. Heterocyclic, aromatic, and aliphatic amines adsorbed on the anodized silver electrode. *J. Electroanal. Chem. Interfacial Electrochem.* **1977**, *84* (1), 1−20.

(9) Albrecht, M. G.; Creighton, J. A. Anomalously intense Raman spectra of pyridine at a silver electrode. *J. Am. Chem. Soc.* **1977**, *99* (15), 5215−5217.

(10) Otto, A. Surface-Enhanced Raman scattering: "Classical" and "Chemical" origins. In *Light Scattering in Solids IV*; Cardona, M.; Guntherodt, G., Eds.; Topics in Applied Physics; Springer: Berlin, 1984; Vol. *54*, pp 289−418.

(11) Moskovits, M. Surface-enhanced spectroscopy. *Rev. Mod. Phys.* **1985**, *57* (3), No. 783.

(12) Moskovits, M. Surface-enhanced Raman spectroscopy: a brief retrospective. *J. Raman Spectrosc.* **2005**, *36* (6−7), 485−496.

(13) Sur, U. K. Surface-enhanced Raman scattering (SERS) spectroscopy: a versatile spectroscopic and analytical technique used in nanoscience and nanotechnology. *Adv. Nano Res.* **2013**, *1*, 111−124.

(14) Nakai, H.; Nakatsuji, H. Electronic mechanism of the surface enhanced Raman scattering. *J. Chem. Phys.* **1995**, *103*, 2286−2294.

(15) Fan, M.; Andrade, G. F.; Brolo, A. G. A review on recent advances in the applications of surface-enhanced Raman scattering in analytical chemistry. *Anal. Chim. Acta* **2020**, *1097*, 1−29.

(16) Xu, L. J.; Zong, C.; Zheng, X. S.; Hu, P.; Feng, J. M.; Ren, B. Label-free Detection of Native Proteins by Surface-enhanced Raman spectroscopy Using Iodide-modified Nanoparticles. *Anal. Chem.* **2014**, *86*, 2238−2245.

(17) Ying, Y.; Tang, Z.; Liu, Y. Material design, development, and trend for surface-enhanced Raman scattering substrates. *Nanoscale* **2023**, *15* (26), 10860−10881.

(18) Wu, Z.; Liu, Y.; Liu, Y.; Xiao, H.; Shen, A.; Zhou, X.; Hu, J. A simple and universal "turn-on" detection platform for proteases based on surface enhanced Raman scattering (SERS). *Biosens. Bioelectron.* **2015**, *65*, 375−381.

(19) Li, Q.; Huo, H.; Wu, Y.; Chen, L.; Su, L.; Zhang, X.; Song, J.; Yang, H. Design and Synthesis of SERS Materials for In Vivo Molecular Imaging and Biosensing. *Adv. Sci.* **2023**, *10* (8), No. 2202051.

(20) Wang, J.; Ahmad, W.; Hassan, M. M.; Zareef, M.; Viswadevarayalu, A.; Arslan, M.; Li, H.; Chen, Q. Landing microextraction sediment phase onto surface enhanced Raman scattering to enhance sensitivity and selectivity for chromium speciation in food and environmental samples. *Food Chem.* **2020**, *323*, No. 126812.

(21) Mekonnen, M. L.; Chen, C. H.; Osada, M.; Su, W. N.; Hwang, B. J. Dielectric nanosheet modified plasmonic-paper as highly sensitive and stable SERS substrate and its application for pesticides detection. *Spectrochim. Acta, Part A* **2020**, *225*, No. 117484.

(22) Muehlethaler, C.; Leona, M.; Lombardi, J. R. Review of surface enhanced Raman scattering applications in forensic science. *Anal. Chem.* **2016**, *88* (1), 152−169.

(23) Singh, D. P.; Herrera, C. E.; Singh, B.; Singh, S.; Singh, R. K.; Kumar, R. Graphene oxide: An efficient material and recent approach for biotechnological and biomedical applications. *Mater. Sci. Eng., C* **2018**, *86*, 173−197.

(24) Panikar, S. S.; Cialla-May, D.; Haaß, T.; Hubner, U.; Gonzalez, A. L.; Salas, P.; Popp, J. Large-scale assembly and pattern transfer of SERS-active nanoparticles for application in drug monitoring of methotrexate in blood serum. *Vib. Spectrosc.* **2023**, *124*, No. 103470.

(25) Ankamwar, B.; Sur, U. K.; Das, P. SERS study of bacteria using biosynthesized silver nanoparticles as the SERS substrate. *Anal. Methods* **2016**, *8* (11), 2335−2340.

(26) Bhattacharjee, G.; Majumder, S.; Senapati, D.; Banerjee, S.; Satpati, B. Core-shell gold @silver hollow nanocubes for higher SERS enhancement and non-enzymatic biosensor. *Mater. Chem. Phys.* **2020**, *239*, No. 122113.

(27) Senapati, D.; Dasary, S. S. R.; Singh, A. K.; Senapati, T.; Yu, H.; Ray, P. C. A Label-Free Gold-Nanoparticle-Based SERS Assay for Direct Cyanide Detection at the Parts-per-Trillion Level. *Chem. - Eur. J.* **2011**, *17*, 8445−8451.

(28) Bhattacharya, M.; Mandal, A. R.; Chakraborty, S. D.; Maiti, A.; Maity, A.; Kuznetsov, D.; Mandal, P.; Senapati, D. Direct Experimental Observation of Salt Induced Aspect Ratio Tunable PFPT Silver-Nanowire Formation: SERS-based ppt Level Hg^{2+} Sensing from Ground Water. *RSC Adv.* **2016**, *6* (51), 45279−45289.

(29) Singh, A. K.; Khan, S. A.; Fan, Z.; Demeritte, T.; Senapati, D.; Senapati, D.; Kanchanapally, R.; Kanchanapally, R.; Ray, P. C. Development of a Long-Range Surface-Enhanced Raman Spectroscopy Ruler. *J. Am. Chem. Soc.* **2012**, *134*, 8662−8669.

(30) Khan, S. A.; Singh, A. K.; Fan, Z.; Senapati, D.; Ray, P. C. Designing distance dependent SERS assay for monitoring photo-thermal antibacterial activity response. *Chem. Commun.* **2012**, *48*, 11091−11093.

(31) Itoh, T.; Prochazka, M.; Dong, Z. C.; Ji, W.; Yamamoto, Y. S.; Zhang, Y.; Ozaki, Y. Toward a new era of SERS and TERS at the nanometer scale: From fundamentals to innovative applications. *Chem. Rev.* **2023**, *123* (4), 1552−1634.

(32) Xu, Y.; Zhang, Y.; Li, C.; Ye, Z.; Bell, S. E. SERS as a Probe of Surface Chemistry Enabled by Surface-Accessible Plasmonic Nanomaterials. *Acc. Chem. Res.* **2023**, *56* (15), 2072−2083.

(33) Yang, B.; Jin, S.; Guo, S.; Park, Y.; Chen, L.; Zhao, B.; Jung, Y. M. Recent development of SERS technology: Semiconductor-based study. *Acs Omega* **2019**, *4* (23), 20101−20108.

(34) Jiang, J.; Bosnick, K.; Maillard, M.; Brus, L. Single molecule Raman spectroscopy at the junctions of large Ag nanocrystals. *J. Phys. Chem. B* **2003**, *107* (37), 9964−9972.

(35) Aravind, P. K.; Nitzan, A.; Metiu, H. The interaction between electromagnetic resonances and its role in spectroscopic studies of molecules adsorbed on colloidal particles or metal spheres. *Surf. Sci.* **1981**, *110* (1), 189−204.

(36) Dey, S.; Mishra, M. S.; Roy, A.; Roy, A.; Senapati, D.; Satpati, B. Multiple Gold Nanoparticle Cores within a Single SiO_2 Shell for Preservable Solid-State Surface-Enhanced Raman Scattering and Catalytic Sensing. *ACS Appl. Nano Mater.* **2023**, *6*, 15606−15619.

(37) Ghosh, A.; De, S. K.; Mondal, S.; Halder, A.; Barai, M.; Guchhait, K. C.; Raul, P.; Karmakar, S.; Ghosh, C.; Patra, A.; Panda, A. K.; Senapati, D.; Sur, U. K. Green synthesis of silver nanoparticles and its applications as sensor, catalyst, and antibacterial agent *Mater. Today: Proc.* 2023 DOI: 10.1016/j.matpr.2023.03.159.

(38) Ghoreishi, S. M.; Behpour, M.; Khayatkashani, M. Green synthesis of silver and gold nanoparticles using Rosa damascena and its primary application in electrochemistry. *Phys. E* **2011**, *44*, 97−104.

(39) Iyer, R. I.; Panda, T. Biogenic synthesis of gold and silver nanoparticles by seed plants. *J. Nanosci. Nanotechnol.* **2014**, *14*, 2024−2037.

(40) Ankamwar, B.; Damle, C.; Ahmad, A.; Sastry, M. Biosynthesis of Gold and Silver Nanoparticles Using Emblica Officinalis Fruit Extract, Their Phase Transfer and Transmetallation in an Organic Solution. *J. Nanosci. Nanotechnol.* **2005**, *5* (10), 1665−1671.

(41) Akintelu, S. A.; Yao, B.; Folorunso, A. S. Green synthesis, characterization, and antibacterial investigation of synthesized gold nanoparticles (AuNPs) from Garcinia kola pulp extract. *Plasmonics* **2021**, *16*, 157−165.

(42) Nayem, S. M. A.; Sultana, N.; Haque, M. A.; Miah, B.; Hasan, M. M.; Islam, T.; Hasan, M. M.; Awal, A.; Uddin, J.; Aziz, M. A.; Ahammad, A. S. Green synthesis of gold and silver nanoparticles by using amorphophalluspaeoniifolius tuber extract and evaluation of their antibacterial activity. *Molecules* **2020**, *25* (20), No. 4773.

(43) Cardoso-Avila, P. E.; Patakfalvi, R.; Rodrlguez-Pedroza, C.; Aparicio-Fernandez, X.; Loza-Cornejo, S.; Villa-Cruz, V.; Martinez-Cano, E. One-pot green synthesis of gold and silver nanoparticles using Rosa canina L. extract. *RSC Adv.* **2021**, *11*, 14624−14631.

(44) Noruzi, M.; Zare, D.; Khoshnevisan, K.; Davoodi, D. Rapid green synthesis of gold nanoparticles using Rosa hybrida petal extract at room temperature. *Spectrochim. Acta, Part A* **2011**, *79*, 1461−1465.

(45) Dubey, S. P.; Lahtinen, M.; Sillanpaa, M. Green synthesis and characterizations of silver and gold nanoparticles using leaf extract of Rosa rugosa. *Colloids Surf., A* **2010**, *364* (1−3), 34−41.

(46) Jha, A. K.; Prasad, K. Rose (Rosa sp.) petals assisted green synthesis of gold nanoparticles. *J. Bionanosci.* **2013**, *7* (3), 245−250.

(47) Frisch, M. J.; Trucks, G. W.; Schlegel, H. B.; Scuseria, G. E.; Robb, M. A.; Cheeseman, J. R.; Scalmani, G.; Barone, V.; Mennucci, B.; Petersson, G. A.; Nakatsuji, H.; Caricato, M.; Li, X.; Hratchian, H. P.; Izmaylov, A. F.; Bloino, J.; Zheng, G.; Sonnenberg, J. L.; Hada, M.; Ehara, M.; Toyota, K.; Fukuda, R.; Hasegawa, J.; Ishida, M.; Nakajima, T.; Honda, Y.; Kitao, O.; Nakai, H.; Vreven, T.; Montgomery, J. A.; Peralta, J. E., Jr.; Ogliaro, F.; Bearpark, M.; Heyd, J. J.; Brothers, E.; Kudin, K. N.; Staroverov, V. N.; Kobayashi, R.; Normand, J.; Raghavachari, K.; Rendell, A.; Burant, J. C.; Iyengar, S. S.; Tomasi, J.; Cossi, M.; Rega, N.; Millam, J. M.; Klene, M.; Knox, J. E.; Cross, J. B.; Bakken, V.; Adamo, C.; Jaramillo, J.; Gomperts, R.; Stratmann, R. E.; Yazyev, O.; Austin, A. J.; Cammi, R.; Pomelli, C.; Ochterski, J. W.; Martin, R. L.; Morokuma, K.; Zakrzewski, V. G.; Voth, G. A.; Salvador, P.; Dannenberg, J. J.; Dapprich, S.; Daniels, A. D.; Farkas, Ö.; Foresman, J. B.; Ortiz, J. V.; Cioslowski, J.; Fox, D. J. *Gaussian 09, Revision D.01*; Gaussian, Inc.: Wallingford CT, 2013.

(48) Grimme, S.; Antony, J.; Ehrlich, S.; Krieg, H. A consistent and accurate ab initio parametrization of density functional dispersion correction (DFT-D) for the 94 elements H-Pu. *J. Chem. Phys.* **2010**, *132*, No. 154104.

(49) Becke, A. D. Density-functional thermochemistry. III. The role of exact exchange. *J. Chem. Phys.* **1993**, *98*, 5648−5652.

(50) Hehre, W. J.; Ditchfield, R.; Pople, J. A. Self-consistent molecular orbital methods. XII. Further extensions of Gaussian-type basis sets for use in molecular orbital studies of organic molecules. *J. Chem. Phys.* **1972**, *56*, 2257−2261.

(51) Hay, P. J.; Wadt, W. R. Ab initio effective core potentials for molecular calculations. Potentials for the transition metal atoms Sc to Hg. *J. Chem. Phys.* **1985**, *82*, 270−283.

(52) Hay, P. J.; Wadt, W. R. Ab initio effective core potentials for molecular calculations. Potentials for K to Au including the outermost core orbitals. *J. Chem. Phys.* **1985**, *82*, 299−310.

(53) Panneerselvam, M.; Jaccob, M. Role of Anation on the Mechanism of Proton Reduction Involving a Pentapyridine Cobalt Complex: A Theoretical Study. *Inorg. Chem.* **2018**, *57*, 8116−8127.

(54) Dzade, N. Y. First-principles insights into the interface chemistry between 4-aminothiophenol and zinc phosphide (Zn_3P_2) nanoparticles. *ACS Omega* **2020**, *5* (2), 1025−1032.

(55) Dang, D. T. X.; Vu, N. H.; Vu, T. T. H.; Thoai, N.; Kawazoe, Y.; Phan, B. T.; Nguyen-Manh, D. Combined density functional theory and boundary element methods study on optical and electronic properties of interfacial Au/TiO_2 defects. *Opt. Mater.: X* **2023**, *20*, No. 100267.

(56) Mhlanga, N.; Ntho, T. A. A theoretical study of 4-Mercaptobenzoic acid assembled on Ag for surface-enhanced Raman scattering applications. *Mater. Today Commun.* **2021**, *26*, No. 101698.

(57) Shahnazari, G. H.; Ganji, M. D. Understanding structural and molecular properties of complexes of nucleobases and Au_{13} golden nanocluster by DFT calculations and DFT-MD simulation. *Sci. Rep.* **2021**, *11* (1), No. 435.

(58) Lu, T.; Chen, F. Multiwfn: A Multifunctional WavefunctionAnalyzer. *J. Comput. Chem.* **2012**, *33*, 580−592.

(59) Zhao, Y.; Zhou, F.; Zhou, H.; Su, H. The structural and bonding evolution in cysteine−gold cluster complexes. *Phys. Chem. Chem. Phys.* **2013**, *15* (5), 1690−1698.

(60) Xu, H.; Kall, M. Polarization-Dependent Surface-Enhanced Raman Spectroscopy of Isolated Silver Nanoaggregates. *ChemPhysChem* **2003**, *4*, 1001−1005.

(61) Xu, H.; Aizpurua, J.; Käll, M.; Apell, P. Electromagnetic contributions to single-molecule sensitivity in surface-enhanced Raman scattering. *Phys. Rev. E* **2000**, *62* (3), No. 4318.

(62) Avouris, P.; Demuth, J. E. Electronic excitations of benzene, pyridine, and pyrazine adsorbed on Ag (111). *J. Chem. Phys.* **1981**, *75* (10), 4783−4794.

(63) Liang, E. J.; Ye, X. L.; Kiefer, W. Surface-enhanced Raman spectroscopy of crystal violet in the presence of halide and halate ions with near-infrared wavelength excitation. *J. Phys. Chem. A* **1997**, *101*, 7330−7335.

(64) Wu, C.; Chen, E.; Wei, J. Surface-enhanced Raman spectroscopy of Rhodamine 6G on agglomerates of different-sized silver truncated nano-triangles. *Colloids Surf., A* **2016**, *506*, 450−456.

(65) Lin, S.; Lin, X.; Lou, X. T.; Yang, F.; Lin, D. Y.; Lu, Z. W.; et al. Rapid and sensitive SERS method for determination of Rhodamine B in chili powder with paper-based substrates. *Anal. Methods* **2015**, *7*, 5289−5294.

(66) Bonancêa, C. E.; do Nascimento, G. M.; De Souza, M. L.; Temperini, M. L.; Corio, P. Substrate development for surface-enhanced Raman study of photocatalytic degradation processes: Congo red over silver modified titanium dioxide films. *Appl. Catal., B* **2006**, *69*, 34−42.